Accepted Manuscript

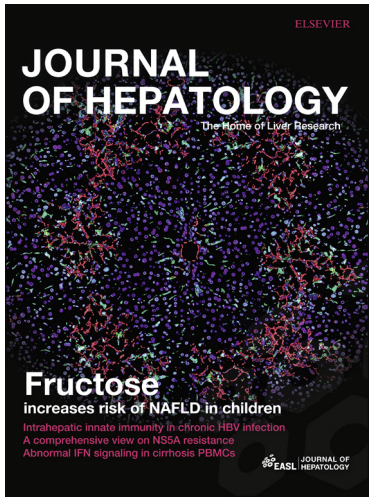

F-actin dynamics regulates mammalian organ growth and cell fate maintenance

Arianna Pocaterra, Giulia Santinon, Patrizia Romani, Irene Brian, Andrea Dimitracopoulos, Andrea Ghisleni, Alejandro Carnicer-Lombarte, Mattia Forcato, Paola Braghetta, Marco Montagner, Francesca Galuppini, Mariaceleste Aragona, Gianmaria Pennelli, Silvio Bicciato, Nils Gauthier, Kristian Franze, Sirio Dupont

PII: S0168-8278(19)30144-8
DOI: https://doi.org/10.1016/j.jhep.2019.02.022
Reference: JHEPAT 7290

To appear in: *Journal of Hepatology*

Received Date: 28 August 2018
Revised Date: 31 January 2019
Accepted Date: 22 February 2019

Please cite this article as: Pocaterra, A., Santinon, G., Romani, P., Brian, I., Dimitracopoulos, A., Ghisleni, A., Carnicer-Lombarte, A., Forcato, M., Braghetta, P., Montagner, M., Galuppini, F., Aragona, M., Pennelli, G., Bicciato, S., Gauthier, N., Franze, K., Dupont, S., F-actin dynamics regulates mammalian organ growth and cell fate maintenance, *Journal of Hepatology* (2019), doi: https://doi.org/10.1016/j.jhep.2019.02.022

JHEPAT-D-18-01600

F-actin dynamics regulates mammalian organ growth and cell fate maintenance

Arianna Pocaterra[1], Giulia Santinon[1], Patrizia Romani[1], Irene Brian[1], Andrea Dimitracopoulos[2], Andrea Ghisleni[3], Alejandro Carnicer-Lombarte[2], Mattia Forcato[4], Paola Braghetta[1], Marco Montagner[1], Francesca Galuppini[5], Mariaceleste Aragona[6], Gianmaria Pennelli[5], Silvio Bicciato[4], Nils Gauthier[2], Kristian Franze[2], and Sirio Dupont[1#]

1. Department of Molecular Medicine DMM, University of Padova, Italy

2. Department of Physiology Development and Neuroscience, University of Cambridge, UK

3. Institute FIRC (Italian Foundation for Cancer Research) of Molecular Oncology (IFOM-FIRC), Milan, Italy

4. Department of Life Sciences, University of Modena and Reggio Emilia, Italy

5. Department of Medicine DIMED, University of Padova, Italy

6. ULB Université Libre de Brussels, Belgium

Corresponding author: sirio.dupont@unipd.it

Keywords:

mechanotransduction; capping protein; CAPZ; F-actin dynamics; YAP; Hippo; organ growth; hepatocyte cell fate maintenance; glucose metabolism; gluconeogenesis; xenobiotic metabolism; liver homeostasis

Electronic word count:

5400 words (Introduction, Methods, Results and Discussion)

Number of figures and tables:

6 Figures, 3 Supplementary Figures, 2 Supplementary Tables (including the CTAT).

Conflict of interest statement:

The authors declare no competing or financial interests.

Financial support statement:

AIRC (Associazione Italiana per la Ricerca sul Cancro) Investigator Grants 15307 and 21392, WCR (Worldwide Cancer Research) Grant 15-1192, CARIPARO Eccellenza Program 2017 and University of Padua BIRD Grant to SD

AIRC 'Hard ROCK Café' Fellowship to GS

Marie Sklodowska-Curie Individual Fellowship (796547) to AG

AIRC Special Program Molecular Clinical Oncology '5 per mille' 10016 to SB

UK Medical Research Council and Sackler Foundation Doctoral Training Grant RG70550 to ACL

UK Medical Research Council Career Development Award G1100312/1 and an Isaac Newton Trust Research Grant 17.24(p) to KF

Author contributions

AP breed mice, performed experiments and analyzed data, with help from GS, PR, IB and MM; PB rederived embryos carrying the targeted *Capzb* allele; MA designed the recombination strategy; FG and GP performed histology and pathological analyses; SB and MF performed bioinformatics analyses; ACL, AD, AP and KF performed AFM and TFM measurements; AG, AP and NG performed TIRF and FRAP experiments; AP and SD planned experiments and wrote the paper.

ABSTRACT

Background & Aims

In vitro, several data indicate that cell function can be regulated by the mechanical properties of cells and of the microenvironment. Cells measure these features by developing forces via their actomyosin cytoskeleton, and respond accordingly by transducing forces into biochemical signals that instruct cell behavior. Among these, the transcriptional coactivators YAP/TAZ recently emerged as key factors mediating multiple responses to actomyosin contractility. However, whether mechanical cues regulate adult liver tissue homeostasis, and whether this occurs through YAP/TAZ, remains largely unaddressed.

Methods & Results

Here we show that the F-actin capping protein CAPZ is a critical negative regulator of actomyosin contractility and mechanotransduction. Capzb inactivation alters stress fiber and focal adhesion dynamics leading to enhanced myosin activity, increased cellular traction forces, and increased liver stiffness. In vitro, this rescues YAP from inhibition by a small geometry; in vivo, inactivation of *Capzb* in the adult mouse liver induces YAP activation in parallel to the Hippo pathway, causing extensive hepatocyte proliferation and leading to striking organ overgrowth. Moreover, *Capzb* is required for the maintenance of the differentiated hepatocyte state, for metabolic zonation, and for gluconeogenesis. In keeping with changes in tissue mechanics, inhibition of the contractility regulator ROCK, or deletion of the *Yap1* mechanotransducer, reverse the phenotypes emerging in *Capzb*-null livers.

Conclusions

These results indicate a previously unrecognized role for CAPZ in tuning the mechanical properties of cells and tissues, which is required in hepatocytes for the maintenance of the differentiated hepatocyte state and to regulate organ size. More in general, it indicates for the first time a physiological role of mechanotransduction in maintaining organ homeostasis in mammals.

LAY SUMMARY

The mechanical properties of cells and tissues (i.e. whether they are soft or stiff) are thought to be important regulators of cell behavior. A recent advancement in our understanding of these phenomena has been the identification of YAP and TAZ as key factors mediating the biological responses of cells to mechanical signals in vitro. However, whether the mechanical properties of cells and/or the mechanical regulation of YAP/TAZ are relevant for mammalian tissue physiology remains unknown. Here we challenge this issue by genetic inactivation of CAPZ, a protein that regulates the cytoskeleton, i.e. the cells' scaffold by which they sense mechanical cues. We found that inactivation of CAPZ alters cells' and liver tissue's mechanical properties, leading to YAP hyperactivation. In turn, this profoundly alters liver physiology, causing organ overgrowth, defects in liver cell differentiation and metabolism. These results reveal a previously uncharacterized role for mechanical signals for the maintenance of adult liver homeostasis.

INTRODUCTION

Cell behavior is powerfully regulated by the mechanical properties of the microenvironment. Seminal studies indicated for example that ECM stiffness and the resulting cell geometry can drive the choice between proliferation, cell death or differentiation, often dominating over soluble cues and oncogenes[1-7]. The current model to explain these observations is that cells probe the physical properties of the microenvironment by exerting contractile forces on adhesion complexes generated by their actomyosin cytoskeleton [8-12]. In turn, actomyosin contractility regulates intracellular signaling pathways to regulate cell behavior.

Several biochemical pathways respond to mechanical cues. Among them, YAP (Yes-associated protein 1) and TAZ (Transcriptional coactivator with PDZ-binding motif or WWTR1) are required mediators of multiple biological responses dictated *in vitro* by mechanical cues and actomyosin contractility[13-15]. YAP/TAZ function as transcriptional coactivators together with the TEAD family of transcription factors, and their activity is regulated by upstream inputs including the Hippo cascade, centered on the LATS1/2 kinases[16,17]. *In vivo*, the function of YAP and of YAP-regulatory inputs has been studied with great detail in the liver tissue, where YAP activation leads to hallmark phenotypes[18-29].

Despite the increasing array of techniques to measure cell's and tissue's mechanical properties[30], a question that remains largely unanswered is whether mechanotransduction and the control of F-actin dynamics is really at work to control adult tissue and organ homeostasis, and whether it does so through YAP or other pathways. Available functional data suggest a role for CAPZ as negative regulator of YAP activity, and as one factor capable of regulating the response of mammary epithelial cells to ECM stiffness *in vitro*[32,41,42]. Yet, how regulation of actin assembly dynamics at the filament barbed end by CAPZ[31] is sufficient to trigger those phenotypes remains unknown. By genetic inactivation in mice we here found an unexpected role for CAPZ in regulating cell contractility and tissue stiffness. This is relevant in adult hepatocytes to restrain YAP activity, such that CAPZ inactivation in the liver leads to organ overgrowth, hepatocyte dedifferentiation and alteration of physiological liver metabolic functions. These phenotypes can be rescued by inhibition of cell contractility and by inactivation of YAP, thus unveiling a role for mechanotransduction in regulating organ size and tissue homeostasis.

METHODS

Mice and treatments

Capzb$^{tm1a(EUCOMM)Wtsi}$ EM:04820 (EUCOMM/EMMA repository) mice were maintained into the C57BL/6N strain. *Yap1fl/fl* and *ROSA26-LSL-LacZ* mice were kindly provided by Dr. Pan. Mice were kept in standard cages with a limit of 5 mice per cage, with ad libitum feeding at an average temperature of 19-24°C. Gender was random. Animal experiments were performed according to our institutional guidelines as approved by the University Animal Welfare Commission (OPBA) and authorized by the Ministry of Health (945/2015-PR and 54/2015-PR). Reporting was according to the ARRIVE guidelines.

The *neo* and *lacZ* cassettes in the Targeted allele (Supplementary Fig. 1A) were removed by crossing with the *CMV-FLP* deleter line, generating *Capzbfl/fl* mice. Subsequent crossing were made to obtain *Albumin–CRE-ERT2; Capzbfl/fl; ROSA26-LSL-lacZ* mice. Mice received 5 consecutive daily i.p. injections of tamoxifen starting at 4-6 weeks of age and analyzed after one month. Control mice were mice of the same genotype but injected with corn oil only, or age-matched littermates without the *CRE* transgene and induced with tamoxifen. Crossing with the *CAGG-CRE* deleter was used to obtain *Capzb+/-* mice, which were born at the expected mendelian ratio. Crossing of *Capzb+/-* mice did not produce any viable *Capzb-/-* offspring (not shown, but significant by chi-squared test). *YAP LKO* mice were *Albumin–CRE-ERT2; Yap1fl/fl; Wwtr1fl/fl; ROSA26-LSL-lacZ*.

For genotyping, mice were anesthetized using isoflurane to surgically remove the tail tip. Genomic DNA was extracted with NaOH at 95°C for 30 minutes, followed by Tris-base pH=8 neutralization. DNA was diluted in water and used for PCR with the following pairs of oligos: *Capzb-floxed*: CAP 71+84; *Capzb-null*: CAP 71+48; *Yap1-floxed*: P1+P2; *Yap1-null*: P1+P3. Primer sequences were CAP 71: AGCCCCTTGTCTGGTAAAAGA; 84: AGCAGAGTAATCAGCTCACCT; 48: CCCCGGAGCATATGAACTGA; YAP P1: CCATTTGTCCTCATCTCTTACTAAC; P2: GATTGGGCACTGTCAATTAATGGGCTT; P3: CAGTCTGTAACAACCAGTCAGGGATAC; CRE: CCTGGAAAATGCTTCTGTCCG, CAGGGTGTTATAAGCAATCCC; lacZ: GGCAGATGCACGGTTACGATGC, CCATGCAGAGGATGATGCTCGTG.

350mg/kg Acetaminophen (APAP, #A7085 Sigma-Aldrich) was injected i.p. in sterile 1XPBS. Serum was collected 8 hours after APAP-injection, livers after 24 hours. Fasudil (LC-laboratories F-4660) was provided in drinking water at an estimated 250mg/kg for 2 weeks, starting together with the first tamoxifen injection.

Hydrodynamic tail vein (HTV) DNA injection

50µg of PiggyBac (PB)-transposon plasmid DNA together with 10µg of hyperactive PB Transposase (hyPBase, Addgene 34879) were diluted in sterile Ringer's solution in a volume corresponding to 10% of the body weight, and injected via the tail vein of 4/6-week-old mice (18-22gr) in a maximum time of 8-10 seconds. PB-CAS9 and PB-RFP-LATS1/2-sgRNA were as in Ref. [32].

Liver sampling

Trans-cardiac perfusion (29-gauge needle) with cold 1XPBS (10-20ml) was performed on euthanized mice to reduce blood contaminants. The liver was placed in 1XPBS on ice, dissected and snap-frozen in liquid nitrogen for extraction of mRNA / proteins, or embedded in OCT and stored at -80°.

Serum measurements

Alanine aminotransferase (ALT) activity was measured in serum using ALT Activity Assay (MAK052 Sigma). Mice were anesthetized with tribromoethyl alcohol (T48402 Sigma) and 2-methyl-2-butanol (240486 Sigma), and blood were collected from the retro-orbital sinus. Blood was clotted at RT for 1 hour and centrifuged for 10 minutes. The serum was stored at -80° for later analysis. Blood glucose levels were measured with CountourXT glucometer (Bayer). IPGTT assays were carried out by intraperitoneal injection of 2mg/g Glucose after overnight starvation.

Antibodies, western blotting and stainings.

CAPZB (SC-81804 for WB, AB6017 Merck for IF), YAP (SC-101199, IF vitro; 13584-1-AP Proteintech, IF in vivo), S19 pMLC (3675 CST, requires permeabilization in -20°C Acetone), CK19 (TROMAIII DSHB, requires OCT inclusion of non fixed tissue), A6 (A6 BCM, DSHB), GS (610517 BD, better on tissues fixed with PFA prior to OCT inclusion), CYP8B1 (SC-101387), pH3 (9701 CST), CD45 (MCA1388 Serotec), HNF4a (SC-6556), HES1 (11988 CST, without tyramide amplification), β-gal (ab9361 Abcam), RFP (10367 Thermofisher), CRE (69050 Millipore), FLAG (F1804 Sigma), GFP (SC-8334), LaminB

(SC-6216), Vinculin (SC-73614), a-Actinin (A7811 Sigma). Secondary isotype-specific anti-mouse labeled IgG were used to decrease background staining.

For immunofluorescence on liver sections, OCT-embedded tissue was cut into 5-8µm thick sections with a Leica CM1950 cryostat. Sections were dried at RT for 30 minutes on a glass coverslip (VWR), and either stored dried at -80°C or directly processed by rehydration in 1XPBS followed by fixation in 4% PFA for 15 minutes. Permeabilization was performed in 1XPBS-Triton 1% for 20 minutes. Blocking was 10% goat serum in 1PBS-Triton 0.5% for 1 hour at RT. CK19-positive area was quantified by measuring the proportion of CK19-positive pixels over the total number of pixels, by using binary thresholded pictures (ImageJ). For phalloidin staining, Alexa Fluor-conjugated phalloidin (Thermofisher) was incubated with secondary antibody in blocking buffer. For histological analysis, paraffin-embedded liver tissue was cut into 5µm sections and stained with hematoxylin-eosin for histologic examination or with Picrosirius Red to visualize fibrosis (commercial kits and protocols). For EdU labelling, mice were injected with 12.5mg/kg of EdU in sterile 1XPBS (A10044 Molecular Probes) 15 hours before tissue sampling. Cells were incubated for 1h with EdU prior to fixation. Liver slice or cells were fixed in PFA 4% and blocked/permeabilised for 30 minutes in 1xPBS 3% BSA + 0.2% Triton (1% Triton for liver slices). EdU reaction mix (100mM Tris pH 8.5, 4mM CuSO4, 625 nM Alexa Azide, 100mM Ascorbic acid) was incubated for 30 minutes, and staining with other antibodies or DAPI was then performed as described above. TUNEL staining was performed according to the DeadEnd™ Fluorometric TUNEL System (Promega). Images were acquired with a Leica SP5 or with a ZEISS LSM700 confocal microscope equipped with CCD camera, using Leica LAS AF or ZEN 2 software, or with a standard Leica DM5000B microscope. Immunofluorescence on cells and western blotting was as in[33].

RNA extraction and gene expression studies

Total liver RNA extractions were performed using Trizol (Thermo) extraction, starting from 5-10mg of liver tissue. Contaminant DNA was removed by RNase free-DNase (Thermo). For cells, total RNA extraction was performed using RNeasy kit (Quiagen) and contaminant DNA was removed by RNase-Free DNase Set (Qiagen). RNA-sequencing was carried out at the CRIBI facility of the University of Padova. Library preparation was

performed using TruSeq Stranded mRNA Library Prep Kit (Illumina) according to the manufacturer's protocol, and sequenced with an Illumina NextSeq 500 platform (75bp, SE, ≥15*10^6 reads/sample). Raw reads were aligned using STAR (version 2.5.3a) [34] to build version mm10 of the mouse genome. Counts for UCSC annotated genes were calculated from the aligned reads using featureCounts function of the Rsubread R package[35] in R-3.3.1. Normalization and differential analysis were carried out using edgeR R package[36]. Raw counts were normalized to obtain Count per Million mapped reads (CPM) and Reads Per Kilobase per Million mapped reads (RPKM). Only genes with a CPM greater than 1 in at least 4 samples were retained for differential analysis.

Retro-transcription was carried out with dT-primed M-MLV Reverse Trascriptase (Thermo). qPCR analyses were carried out with triplicates of each sample cDNA on QuantStudio 6 Flex Real-Time PCR System (Thermo) with a FastStart SYBR Green Master Mix (Roche). Expression levels were calculated relative to *GAPDH* based on the efficiency^-ΔCt method. qPCR primer sequences were GAPDH: ATCCTGCACCACCAACTGCT, GGGCCATCCACAGTCTTCTG; ANKRD1: CTGTGAGGCTGAACCGCTAT, TCTCCTTGAGGCTGTCGAAT; CYR61: GCTCAGTCAGAAGGCAGACC, GTTCTTGGGGACACAGAGGA; BICC1: CTCGCAGCCAACATATGTCC, GTTGGCTCTCCTCAGTTCCT; TAGLN2: AGCAGATCCTCATCCAGTGG, CCATCTGCTTGAAGGCCATC.

Cell lines

Primary mouse adult fibroblasts (MAFs), were obtained by standard procedures after enzymatic digestion of the tail-tip and plated in DMEM+20% FBS, 1% Gln, Pen/Strep. MAFs were kept in a low-oxygen (5%) incubator to prevent stress-induced senescence. Subsequent manipulations and experiments were performed in a standard incubator. Cells were routinely tested negative for mycoplasma contamination (ATCC Kit). Plasmid DNA (GFP-Actin, mCherry-Vinculin) was electroporated according to the manufacturer's instructions. Viral infections (Adeno-empty UIowa-272 and Adeno-CRE UIowa-5) were carried out following standard procedures and protocols.

Microfabrications

Substrates were made of polyacrylamide (PAA), polymerized on standard 25mm glass coverslips. (3-Aminopropyl) trimethoxysilane (APTMS) was applied to the glass surface for 3min, followed by washes with ddH2O, and treatment with 0.5% glutaraldehyde for 30min. A pre-mixed solution was made of 500µl 40% acrylamide, 65µl 100% hydroxy-acrylamide and 250µl 2% bis-acrylamide (Bis-AA, Fisher scientific), and diluted in PBS to obtain the desired stiffness. After 15min de-gassing, TEMED and APS were added to initiate the cross-linking, and 50µl of the solution immediately pipetted on the coverslips. A plasma-cleaned coverslip made hydrophobic with RainX (Kraco Car Care International Ltd.) was lowered onto the drop to ensure even thickness; this was later covered with PBS and removed. The gels were washed in PBS and sterilized under UV light. Gels were treated with 100µg/ml poly-D-lysine (PDL) overnight, and then with Fibronectin for 1 hour to promote cell adhesion. All chemicals were from Sigma-Aldrich, unless otherwise stated. Micropatterned glass slides[13] were from Cytoo SA (PADO-1 custom mask, available to all users upon request). For each slide, 80.000 cells were plated in a 6-well plate dish containing a single slide, and non-adherent cells were washed with medium after 2 hr.

Fluorescence Recovery After Photo-bleaching (FRAP)

24 hours after transfection (mCherry-Vinculin or GFP-Actin), MAFs were re-seeded on glass-bottom dishes (Matek, Sigma-Aldrich) coated with 10µg/ml fibronectin, and imaged in Ringer's phenol-red free medium upon complete spreading with a Confocal Spinning Disk microscope (Olympus) equipped with a 100x/1.35Sil silicone oil immersion objective, a iXon897 Ultra camera (ANDOR) and a FRAP module equipped with a 405nm laser. Environmental control was maintained with an OKOlab incubator. Circular Regions Of Interest (ROI) of 2µm diameter were photo-bleached at 50% intensity for Actin and 100% intensity for Vinculin, and post-bleaching images were followed with 15 to 20% laser intensity for 100 frames (1 frame every second for Actin, every 0.5 seconds for Vinculin). FRAP data were analyzed as reported[37] and curves fitted to a monoexponential recovery equation by the Graphpad Prism software: $I= I_0+Imax*[1-e^{-(k)*(t)}]$

Where I is the relative intensity compared to the pre-bleaching value, k represents the association rate constant, and t is expressed in seconds.

Total Internal Reflection Fluorescence (TIRF) microscopy

TIRF microscopy of MAFs was performed using a DMI6000B equipped with AM TIRF module (Leica). Images were acquired using either a PlanApoN 60× 1.45-NA or UApoN 100× 1.49-NA TIRF oil-immersion objective, captured using a Ixon+ EMCCD camera (Andor). All images were acquired with the same camera settings and laser intensity for consistent image analysis. A custom macro, available upon request, was designed to quantify the number and size of focal adhesions per cell. Images containing a single cell were background-subtracted and a binary mask was created by applying non-linear filters. The mask was then applied on raw images to obtain particle sizes and area. Only particle sizes >200nm^2 were considered in the analysis, as this avoided analysis of background particles. All images were acquired with the same settings and consistently analyzed by concatenating all images, while saturated images were discarded.

Traction Force Microscopy (TFM)

Preparation of Polyacrylamide (PAA) Substrates. PAA gels were prepared on imaging dishes (µ-Dish, Ibidi, Germany) as previously described[38]. Fluorescent nanoparticles (FluoSpheres carboxylate, 0.2 µm, crimson, Life Technologies, UK) were added to the PAA pre-mixes, which were then placed in an ultrasonic bath for 30s to separate the beads. After starting polymerisation, the imaging dish was inverted to ensure that beads settled close to the gel surface.

Time Lapse Imaging for TFM. MAFs were seeded onto PAA gels with shear storage moduli *G'* of 1 kPa ('soft') and 10 kPa ('stiff'). After 24 hours, cells where imaged using an inverted microscope (Leica DMi8) at 37°C and 5% CO_2, equipped with a digital sCMOS camera (ORCA-Flash4.0, Hamamatsu Photonics), an EL6000 illuminator (Leica, Germany), and a 63x oil objective (NA1.4, Leica, Germany). Images were acquired using Leica LAS X software. Fluorescence images of beads, and widefield images of cells were taken every 2 minutes. After image acquisition, culture media were exchanged with Trypsin-EDTA (Gibco) to detach cells from the gel. Reference images of fluorescent beads were taken 15 min after trypsinisation. Three independent traction force experiments were performed for each condition.

Data Analysis for TFM. Traction stress maps were calculated for each frame using a TFM Software Package in ImageJ[39]. To minimize noise, regularisation parameters of 0.01 and 0.00001 were chosen for cells on 1 kPa and 10 kPa PAA gels, respectively Traction stresses were averaged over time for each cell. Post-processing of the data and

statistical analyses were done with a custom Python script. The distributions of the average stresses were compared using Mann-Whitney tests.

Atomic Force Microscopy (AFM)

All AFM experiments were performed in accordance with the UK Animals (Scientific Procedures) Act 1986. Mice were sacrificed via an approved schedule 1 method. Livers were immediately dissected and embedded in low melting point agarose (4% in PBS; Sigma Aldrich). A small block of agarose containing the sample was submerged in chilled PBS and cut into 500 µm thick sections using a vibratome (Leica). Sections were slowly heated to 37 °C in PBS for 30 min prior to AFM measurements. AFM measurements were carried out similarly as previously described[40]. Monodisperse polystyrene beads (radius r = 18.64 µm ± 0.17 µm, microParticles GmbH, Berlin, Germany) were glued to tipless silicon cantilevers (spring constants between 0.01 and 0.03 N/m; Arrow-TL1, NanoWorld, Neuchatel, Switzerland). The AFM was mounted on an x/y motorized stage of an inverted microscope (AxioObserver A1, Zeiss, Cambridge, UK). Cantilever position relative to the liver sections was monitored via a CCD camera (The Imaging Source, Bremen, Germany) placed on top of the AFM setup. Force-distance curves were taken with a set force of 10nN with an approach speed of 10µm s-1. Apparent elastic moduli K were calculated using the Hertz model: $F = 4/3\ K\ r^{1/2}\ \delta^{3/2}$ for an indentation depth δ = 2 µm, using a custom written automated algorithm based in Matlab (MathWorks, Natick, USA). Stiffness was measured in maps over defined sample areas, over which multiple force-distance curves were taken at 20 µm steps (each map containing 40-200 measurements, 2-3 maps per liver). The median measurement stiffness for each map was calculated, and statistical significance between maps was determined using a two-tailed Student's t-test.

Statistical analysis

Data analyses were performed using GraphPad Prism software. Graphs indicate mean values and single values of all biological replicates (or mice), unless otherwise indicated. Data for each mouse derive from analysis of multiple (n≥6) tissue sections. To facilitate gene expression data visualization, the mean expression levels in WT mice was set equal to 1, and all other data (single values, means and errors) are relative to this. Significance was calculated by applying unpaired Wilcoxon-Mann-Whitney tests (n=3 samples) or

Student's t-tests (n≥4 samples); for RNA sequencing, we considered as significant only genes with $P<0.05$.

Data availability

Data that support the findings is available in the manuscript or upon reasonable request to the corresponding author. RNA seq data have been deposited in GEO database (GSE116993). See also Supplementary CTAT Table.

RESULTS

Derivation and validation of a *Capzb* floxed allele.

To functionally dissect the role of mechanotransduction and F-actin dynamics *in vivo*, we chose to inactivate the F-actin capping protein CAPZ. CAPZ is a dimer whose alpha subunit is encoded by two loci in mammals (*Capza1* and *Capza2*), while the beta subunit is encoded by only one gene (*Capzb* - Gene ID: 12345), facilitating genetic analysis. We thus recombined the *Capzb*$^{tm1a(EUCOMM)Wtsi}$ allele to obtain *Capzb-floxed* mice (see Methods and Supplementary Fig. 1A-B); the same allele was recently used in Ref. [41]. We validated this allele by monitoring efficient depletion of the endogenous CAPZB protein in primary adult *Capzb-fl/fl* fibroblasts recombined by adenoviral-CRE infection (Supplementary Fig. 1C). Moreover, adenoviral-CRE recombination of primary newborn *Capzb-fl/fl* cardiomyocytes led to a rapid disassembly of contractile actomyosin structures (Supplementary Fig. 1D), in line with the role of CAPZ in muscle sarcomeres[31]. We speculate this defect might underlie the lethality of *Capzb-/-* embryos (see methods).

We also aimed at specifically validating the role of CAPZ in the context of mechanotransduction. For this we compared the biological response of *WT* (*Capzbfl/fl* + adeno-control) and *CAPZ KO* (*Capzbfl/fl* + adeno-Cre) primary adult fibroblasts (MAFs) to mechanical cues: *WT* MAFs respond to a small cell geometry, which is associated to decreased actomyosin contractility[42], by inactivating YAP/TAZ and by decreasing proliferation (Fig. 1A and B), in line with Ref. [13,14]; in contrast, *CAPZ KO* MAFs retained nuclear YAP and kept proliferating, at least to a certain extent (Fig. 1A and B). As a control, *CAPZ KO* MAFs completely detached from the substratum maintain YAP nuclear exclusion (not shown). Thus, *Capzb* is required in MAFs for the inhibition of YAP in conditions of decreased contractility.

Capzb limits actomyosin contractility in response to ECM mechanical cues

We then sought to understand at what level does CAPZ act to regulate mechanotransduction. We analyzed F-actin and focal adhesions (FAs) in WT and *CAPZ KO* MAFs, as these are critically involved in cell mechanics. Phalloidin staining on fixed cells indicated thinner and denser bundles in *CAPZ KO* MAFs (Fig. 1C). FRAP (Fluorescence Recovery After Photobleaching) analysis of Actin dynamics in stress fibers indicated a faster recovery in *CAPZ KO* cells (Fig. 1D), and thus a faster actin turnover

previously associated to higher levels of Myosin-II activity[43,44]. Analysis of Vinculin dynamics in focal adhesions (FAs) indicated a slower recovery in *CAPZ KO* cells (Fig. 1E), and thus more stable Vinculin, a typical feature observed upon increased pulling forces or upon stiffening of the ECM[45-48]. This was associated with a higher number of Vinculin-positive FAs, but of smaller size (Fig. 1F). During these analyses we noted a redistribution of FAs from predominantly peripheral to a more central position, perhaps reminiscent of the recently-described perinuclear FAs specifically associated to increased tension and YAP activity[49]; to quantify this phenotype we plated MAFs on cross-bow shaped fibronectin micropatterns and averaged the intensity of the staining over several stacked cells[50,51], confirming our observation (Fig. 1G). Furthermore, *CAPZ KO* MAFs display increased levels of active S19-phosphorylated myosin light chain (pMLC - Fig.1H), and increased cellular forces on stiff hydrogels (*G'* = 10kPa), as measured by traction force microscopy (Fig. 1I). Finally, we extended these findings in the context of a soft ECM microenvironment, where CAPZ inactivation is relevant to regulate YAP/TAZ[52]: pMLC staining was almost undetectable in MAFs on soft hydrogels (*G'* = 1kPa), but clearly visible in *CAPZ KO* MAFs (Fig. 1J). Moreover, *CAPZ KO* MAFs exerted significantly higher forces on their substratum also in this condition compared to control cells (Fig. 1K). Collectively, these data indicate that deletion of *Capzb* enables the development of higher cellular forces even in conditions of decreased extracellular resistance, unveiling a previously unsuspected role for CAPZ. Moreover, this validates *Capzb* inactivation as a meaningful tool to modulate F-actin dynamics and cell mechanics *in vivo*.

Conditional inactivation of *Capzb* in hepatocytes activates the YAP mechanotransducer

To probe a role of *Capzb* as regulator of tissue physiology we focused on the liver, because hepatocytes are inherently mechanosensitive[1,53] and because it is a model system for Hippo/YAP [54-56]. We thus obtained *Albumin-CRE-ERT2; Capzb-fl/fl; ROSA26-LoxSTOPLox-lacZ* mice (hereafter, *CAPZ LKO*) to delete *Capzb* in adult hepatocytes in a time-controlled manner, and enabling the lineage tracing of recombined cells by beta-galactosidase expression (Fig. 2A, Supplementary Fig. 2A and B).

We initially sought to find evidence for activation of the YAP mechanotransducer in *CAPZ LKOs*. We monitored a series of established YAP target genes in the liver tissue[18,26], and found them upregulated in *Capzb*-null livers (Fig. 2B). Similarly, we

performed a more global analysis of gene expression and found that genes activated in *CAPZ LKOs* are remarkably overlapping with those activated in *Hippo*-mutants[26,28,57] and *Yap*-transgenics[18,20,58] (Fig. 2C). Prompted by these results, we directly monitored endogenous YAP localization by immunofluorescence, and found increased nuclear localization in *Capzb*-null hepatocytes (Fig. 2D and Supplementary Fig. 2H). Of note, mutant liver tissues also display an overall increase in YAP staining intensity (Fig. 2E).

Control of liver organ size by inactivation of *Capzb*

Phenotypically, inactivation of *Capzb* caused an evident hepatomegaly reaching on average 200% of the normal liver/body weight ratio (Fig. 2F). Hepatocytes appeared enlarged, similarly to what observed in *Lats1/2* knockouts[26] (see Supplementary Fig. 2A), and exhibited a stark increase in proliferation as measured by EdU incorporation (i.e. S-phase) and phospho-Histone3 (i.e. mitosis) staining (Fig. 2G and H and Supplementary Fig. 2C). This was accompanied by overexpression of several proliferation markers (Fig. 2I), including known direct YAP targets[58,59], and of antiapoptotic genes (Supplementary Fig. 2D). As control, we excluded major alterations of cell-cell junctions (Supplementary Fig. 2E), previously observed by *CAPZ* inactivation in flies[60], fibrosis (see Supplementary Fig. 2A) and inflammation (Supplementary Fig. 2F and G). This indicated that CAPZ is required in adult hepatocytes to keep control over a key mechanotransduction pathway, and that it potently restrains hepatocyte proliferation.

***Capzb* controls liver cell fate**

Activation of YAP in hepatocytes leads to expansion of atypical ductal cells (ADCs) / oval cells / biliary epithelial cells (BECs) that display bipotent progenitor identity[20,23]. Analysis of *CAPZ LKO* livers indicated a massive expansion of A6- and CK19-positive ADCs forming disorganized strands in the liver parenchyma, mainly distributed around the portal area (Fig. 3A), and this was accompanied by increased expression of cholangiocyte/progenitor markers[20,61] in *CAPZ LKO* livers (Fig. 3B). Appearance of ADCs upon YAP activation has been attributed to dedifferentiation of hepatocytes, with appearance of cells double-positive for CK19 and HNF4α (markers for the cholangiocyte and hepatocyte lineages, respectively) [20], which we also found in *CAPZ LKO* livers (Fig. 3C). Moreover, in keeping with a role for Notch in regulating hepatocyte

dedifferentiation[20,62], we found the Notch pathway activated in *CAPZ LKO* livers (Fig. 3D and E). To unequivocally trace ADCs to hepatocytes bearing *Capzb* deletion, we performed a double staining for beta-galactosidase (which labels recombined hepatocytes) and CK19, and found co-localization (Fig. 3F). Of note, this indicated dedifferentiation of hepatocytes also at a distance from the portal area. As an alternative approach, we expressed a *Cre* transgene in hepatocytes of *Capzb-fl/fl* mice by hydrodynamic tail vein (HTV) transposon DNA injection[63], which caused appearance of cells doubly positive for CK19 and beta-galactosidase (Fig. 3G). This indicates a cell-autonomous function of *Capzb*. More in general, these data indicate that *Capzb* inactivation is sufficient to reprogram adult hepatocyte fate.

Capzb controls hepatocyte zonation and liver metabolism

Metabolism in the liver parenchyma is zonated, with hepatocytes expressing different metabolic genes along the periportal to pericentral axis of the hepatic lobules in response to several signaling cues[64-66]. Recent evidence indicates that YAP activity contributes to zonation by inhibiting pericentral gene expression[28]. We thus checked for expression of established pericentral markers in *CAPZ LKO* livers, and found them strikingly reduced both at the mRNA level (Fig. 4A) and by immunostaining (Fig. 4B and C). Pericentral zonation is particularly evident if looking at the expression of cytochromes involved in xenobiotic metabolism[66,67]. Among these we focused our attention on *Cyp1A2* and *Cyp2E1*, the main genetic determinants of acetaminophen (APAP) toxicity in the mouse[68], which we found strongly inhibited (see Fig. 4A). Reflecting decreased expression, we then found that *CAPZ LKO* were extremely resistant to APAP intoxication: at sub-lethal doses (350mg/Kg) sufficient to cause extensive cell death (as measured by TUNEL assay) and extensive hepatic damage (as measured by serum ALT) in *WT* mice, *CAPZ LKO* mice remained insensitive (Fig. 4D and E).

Another recently reported function of YAP in the liver is the regulation of gluconeogenesis and blood glucose homeostasis[29]. Accordingly, we found decreased expression of key gluconeogenic genes in *CAPZ LKO* mice (Fig. 4F), and this was functionally linked to decreased steady-state blood glucose levels and improved glucose tolerance (Fig. 4G). Overall, these data indicate that *Capzb* is relevant to maintain the physiological patterning of hepatocyte differentiation and of key metabolic traits in the liver.

Capzb regulates liver homeostasis through YAP

To obtain formal evidence that phenotypes observed upon *Capzb* inactivation are due to YAP activation, and not to other mechanoresponsive pathways, we deleted *Yap1*[22] in *CAPZ LKOs* (*Albumin-CreERT2; Capzb-fl/fl; Yap1-fl/fl; ROSA26-LSL-lacZ* mice, *CAPZ+YAP LKO*). As shown in Fig. 5A-E and Supplementary Fig. 3A, *Yap1* inactivation partially rescued hepatomegaly and proliferation, while it almost completely rescued atypical ductal cell expansion, pericentral expression, and glucose tolerance. We speculate the partial rescue might depend on TAZ, which is functional in hepatocytes[69] and sufficient to induce hepatocyte proliferation (see Fig. 5G). This would also imply that the phenotypes described above require different thresholds of YAP/TAZ activity. Thus, the control of F-actin assembly dynamics is a physiologically-relevant input to keep control over YAP/TAZ activity in the liver.

Capzb regulates YAP/TAZ in parallel to Hippo

Some data suggest that mechanical regulation of YAP/TAZ involve YAP phosphorylation by LATS kinases; functional data however indicate that mechanical regulation of YAP/TAZ can occur in the absence of LATS1/2[15]. The effectiveness of *Capzb* inactivation in regulating YAP/TAZ in hepatocytes offered us the opportunity to test the genetic interaction with *Lats1/2 in vivo*. We thus expressed in the liver, by HTV transposon injection, the CAS9 enzyme and guide-RNAs targeting *Lats1* and *Lats2*[32], to inactivate *Lats1/2* without inducing liver failure caused by whole-organ knockout[26,70]. CRISPR inactivation of *Lats1/2* induced multiple *YAP*-dependent phenotypes (Supplementary Fig. 3B-D), indicating efficient recombination of both genes[26,32,71,72]. We then found that the combination of *Capzb* and *Lats1/2* inactivation induced a higher number of proliferating cells compared to *Lats1/2* inactivation alone (Fig. 5F and Supplementary Fig. 3E), ruling out the possibility that CAPZ works only through LATS1/2 to regulate YAP. We also injected a transposon plasmid encoding for TAZ-4SA (a TAZ isoform that cannot be phosphorylated and inhibited by LATS kinases) and obtained a comparable cooperation with *Capzb* deletion (Fig. 5G and Supplementary Fig. 3F). Overall this indicates that regulation of YAP/TAZ by actin assembly dynamics regulates YAP in parallel to the Hippo cascade also in the liver tissue[13,52,73,74].

Capzb regulates liver homeostasis by controlling tissue mechanics

Data gathered so far indicate that *Capzb* regulates cellular forces in vitro, and the activity of a key mechanotransduction pathway in vivo. We then sought to test the idea that CAPZ regulates tissue mechanical properties also in vivo. For this we monitored F-actin and MLC phosphorylation[75] and found them increased in *CAPZ LKO* liver tissue compared to the controls (Fig. 6A). Importantly, this was associated to increased tissue stiffness, which can be an indirect readout of actomyosin contractility in cells[76], as measured by atomic force microscopy (Fig. 6B). Moreover, target genes that are inhibited in hepatocytes subjected to high stiffness[1,53] are downregulated in *CAPZ LKO* livers (Fig. 6C), further supporting the view that CAPZ regulates the cell's mechanical properties. To functionally validate these findings, we inhibited ROCK activity in *CAPZ LKO* mice, which efficiently reduced MLC phosphorylation (Fig. 6D), and scored YAP-dependent phenotypes. As shown in Fig. 6E-G, hallmark phenotypes induced by *Capzb* deletion, including expression of direct YAP target genes, were inhibited by Fasudil treatment. Altogether, these data indicate a function of *Capzb* in restraining tissue tension, and a physiological role for tissue tension in regulating hepatocyte homeostasis.

DISCUSSION

Here we found that inactivation of the capping protein *Capzb* induced increased cell tension and tissue stiffness, and enabled pMLC activity in soft environments which would normally suppress it, including the liver[53]. *Capzb* inactivation induced liver overgrowth, hepatocyte dedifferentiation and repatterning of liver metabolism, which all depend on the YAP mechanotransduction pathway. These phenotypes were similar in strength, and overlapping by gene expression analyses, with published liver mutants of the Hippo pathway, and can be readily seen by inactivating *Capzb* in adult hepatocytes. We also found that *Capzb* and Hippo inactivation cooperate to drive hepatocyte proliferation, genetically supporting the view that mechanical signals regulate YAP/TAZ through both LATS-dependent[77] and LATS-independent mechanisms[78,79]. This makes CAPZ the only genetically-validated YAP/TAZ regulator from flies[80,81] to mammals besides the Hippo pathway. We did not find evidence for a mechanical activation of beta-catenin though[82], because zonation defects are compatible, if anything, with inhibited beta-catenin[64].

Our results suggest that capping of the F-actin barbed end is crucial to regulate cell mechanics in vitro and in vivo, and a required determinant of adult liver homeostasis. The phenotypes observed in *Capzb*-null livers were stable up to 30 weeks (not shown), suggesting that the novel function that we describe here for CAPZ cannot be easily compensated, and that CAPZ plays a prominent role in regulating cell and tissue mechanotransduction. These results now open the interesting possibility that CAPZ levels and activity are regulated in tissues, eventually contributing to pattern cell mechanics, YAP/TAZ and perhaps other mechanotransduction pathways. The existence of a whole family of CAPZ-regulatory proteins and the known but so far poorly addressed role of phosphoinositides as regulators of CAPZ[31] represent a possible basis to better understand in future how CAPZ activity, and by association F-actin assembly dynamics, are involved in signaling mechanisms maintaining tissue homeostasis.

ACKNOWLEDGEMENTS

We thank Dr. Duojia Pan and Dr. Stefano Piccolo for mice, Dr. Bin Zhao for the generous gift of plasmids and protocols, Dr. Antonio Rosato for help in establishing HTV injections, Dr. Guillaume Charras for sharing IF protocol for pMLC. This work was supported by AIRC (Associazione Italiana per la Ricerca sul Cancro) Investigator Grant 15307, WCR (Worldwide Cancer Research) Grant 15-1192, CARIPARO Eccellenza Program 2017 and University of Padua BIRD Grant to SD, AIRC 'Hard ROCK Café' Fellowship to GS, Marie Sklodowska-Curie Individual Fellowship (796547) to AG, AIRC Special Program Molecular Clinical Oncology '5 per mille' 10016 to SB, UK Medical Research Council and Sackler Foundation Doctoral Training Grant RG70550 to ACL, UK Medical Research Council Career Development Award G1100312/1 and an Isaac Newton Trust Research Grant 17.24(p) to KF.

REFERENCES

[1] Mooney D, Hansen L, Vacanti J, Langer R, Farmer S, Ingber D. Switching from differentiation to growth in hepatocytes: control by extracellular matrix. J Cell Physiol 1992;151:497–505. doi:10.1002/jcp.1041510308.

[2] Chen CS, Mrksich M, Huang S, Whitesides GM, Ingber DE. Geometric control of cell life and death. Science (New York, NY) 1997;276:1425–8.

[3] McBeath R, Pirone DM, Nelson CM, Bhadriraju K, Chen CS. Cell Shape, Cytoskeletal Tension, and RhoA Regulate Stem Cell Lineage Commitment 2004;6:483–95. doi:10.1016/S1534-5807(04)00075-9.

[4] Engler AJ, Sen S, Sweeney HL, Discher DE. Matrix elasticity directs stem cell lineage specification. Cell 2006;126:677–89. doi:10.1016/j.cell.2006.06.044.

[5] Watt FM, Jordan PW, O'Neill CH. Cell shape controls terminal differentiation of human epidermal keratinocytes. Proc Natl Acad Sci USa 1988;85:5576–80.

[6] Weaver VM, Petersen OW, Wang F, Larabell CA, Briand P, Damsky C, et al. Reversion of the malignant phenotype of human breast cells in three-dimensional culture and in vivo by integrin blocking antibodies. J Cell Biol 1997;137:231–45.

[7] Paszek MJ, Zahir N, Johnson KR, Lakins JN, Rozenberg GI, Gefen A, et al. Tensional homeostasis and the malignant phenotype. Cancer Cell 2005;8:241–54. doi:10.1016/j.ccr.2005.08.010.

[8] Schwartz MA. Integrins and extracellular matrix in mechanotransduction. Cold Spring Harbor Perspectives in Biology 2010;2:a005066. doi:10.1101/cshperspect.a005066.

[9] Iskratsch T, Wolfenson H, Sheetz MP. Appreciating force and shape—the rise of mechanotransduction in cell biology. Nat Rev Mol Cell Biol 2014;15:825–33. doi:10.1038/nrm3903.

[10] Vogel V. Unraveling the Mechanobiology of Extracellular Matrix. Annu Rev Physiol 2018;80:353–87. doi:10.1146/annurev-physiol-021317-121312.

[11] Vining KH, Mooney DJ. Mechanical forces direct stem cell behaviour in development and regeneration. Nat Rev Mol Cell Biol 2017. doi:10.1038/nrm.2017.108.

[12] Sun Z, Guo SS, Fässler R. Integrin-mediated mechanotransduction. J Cell Biol 2016;215:445–56. doi:10.1083/jcb.201609037.

[13] Dupont S, Morsut L, Aragona M, Enzo E, Giulitti S, Cordenonsi M, et al. Role of YAP/TAZ in mechanotransduction. Nature 2011;474:179–83. doi:10.1038/nature10137.

[14] Wada K-I, Itoga K, Okano T, Yonemura S, Sasaki H. Hippo pathway regulation by cell morphology and stress fibers. Development 2011;138:3907–14. doi:10.1242/dev.070987.

[15] Dupont S. Role of YAP/TAZ in cell-matrix adhesion-mediated signalling and mechanotransduction. Exp Cell Res 2016;343:42–53. doi:10.1016/j.yexcr.2015.10.034.

[16] Piccolo S, Dupont S, Cordenonsi M. The biology of YAP/TAZ: hippo signaling and beyond. Physiol Rev 2014;94:1287–312. doi:10.1152/physrev.00005.2014.

[17] Johnson R, Halder G. The two faces of Hippo: targeting the Hippo pathway for regenerative medicine and cancer treatment. Nat Rev Drug Discov 2014;13:63–79. doi:10.1038/nrd4161.

[18] Dong J, Feldmann G, Huang J, Wu S, Zhang N, Comerford SA, et al. Elucidation of a universal size-control mechanism in Drosophila and mammals. Cell 2007;130:1120–33. doi:10.1016/j.cell.2007.07.019.

[19] Camargo FD, Gokhale S, Johnnidis JB, Fu D, Bell GW, Jaenisch R, et al. YAP1

increases organ size and expands undifferentiated progenitor cells. Current Biology : CB 2007;17:2054–60. doi:10.1016/j.cub.2007.10.039.
[20] Yimlamai D, Christodoulou C, Galli GG, Yanger K, Pepe-Mooney B, Gurung B, et al. Hippo pathway activity influences liver cell fate. Cell 2014;157:1324–38. doi:10.1016/j.cell.2014.03.060.
[21] Benhamouche S, Curto M, Saotome I, Gladden AB, Liu C-H, Giovannini M, et al. Nf2/Merlin controls progenitor homeostasis and tumorigenesis in the liver. Genes Dev 2010;24:1718–30. doi:10.1101/gad.1938710.
[22] Zhang N, Bai H, David KK, Dong J, Zheng Y, Cai J, et al. The Merlin/NF2 tumor suppressor functions through the YAP oncoprotein to regulate tissue homeostasis in mammals. 2010;19:27–38. doi:10.1016/j.devcel.2010.06.015.
[23] Lu L, Li Y, Kim SM, Bossuyt W, Liu P, Qiu Q, et al. Hippo signaling is a potent in vivo growth and tumor suppressor pathway in the mammalian liver. Proc Natl Acad Sci USa 2010;107:1437–42. doi:10.1073/pnas.0911427107.
[24] Zhou D, Conrad C, Xia F, Park J-S, Payer B, Yin Y, et al. Mst1 and Mst2 Maintain Hepatocyte Quiescence and Suppress Hepatocellular Carcinoma Development through Inactivation of the Yap1 Oncogene. Cancer Cell 2009;16:425–38. doi:10.1016/j.ccr.2009.09.026.
[25] Lee K-P, Lee J-H, Kim T-S, Kim T-H, Park H-D, Byun J-S, et al. The Hippo-Salvador pathway restrains hepatic oval cell proliferation, liver size, and liver tumorigenesis. Proc Natl Acad Sci USa 2010;107:8248–53. doi:10.1073/pnas.0912203107.
[26] Lee D-H, Park JO, Kim T-S, Kim SK, Kim T-H, Kim M-C, et al. LATS-YAP/TAZ controls lineage specification by regulating TGFβ signaling and Hnf4α expression during liver development. Nat Comms 2016;7:11961. doi:10.1038/ncomms11961.
[27] Nishio M, Sugimachi K, Goto H, Wang J, Morikawa T, Miyachi Y, et al. Dysregulated YAP1/TAZ and TGF-β signaling mediate hepatocarcinogenesis in Mob1a/1b-deficient mice. Proceedings of the National Academy of Sciences 2016;113:E71–80. doi:10.1073/pnas.1517188113.
[28] Fitamant J, Kottakis F, Benhamouche S, Tian HS, Chuvin N, Parachoniak CA, et al. YAP Inhibition Restores Hepatocyte Differentiation in Advanced HCC, Leading to Tumor Regression. CellReports 2015;10:1692–707. doi:10.1016/j.celrep.2015.02.027.
[29] Hu Y, Shin DJ, Pan H, Lin Z, Dreyfuss JM, Camargo FD, et al. YAP suppresses gluconeogenic gene expression through PGC1α. Hepatology 2017;66:2029–41. doi:10.1002/hep.29373.
[30] Roca-Cusachs P, Conte V, Trepat X. Quantifying forces in cell biology. Nat Cell Biol 2017;19:742–51. doi:10.1038/ncb3564.
[31] Edwards M, Zwolak A, Schafer DA, Sept D, Dominguez R, Cooper JA. Capping protein regulators fine-tune actin assembly dynamics. Nat Rev Mol Cell Biol 2014;15:677–89. doi:10.1038/nrm3869.
[32] Guo X, Zhao Y, Yan H, Yang Y, Shen S, Dai X, et al. Single tumor-initiating cells evade immune clearance by recruiting type II macrophages. Genes Dev 2017;31:247–59. doi:10.1101/gad.294348.116.
[33] Santinon G, Brian I, Pocaterra A, Romani P, Franzolin E, Rampazzo C, et al. dNTP metabolism links mechanical cues and YAP/TAZ to cell growth and oncogene-induced senescence. Embo J 2018;37:e97780. doi:10.15252/embj.201797780.
[34] Dobin A, Davis CA, Schlesinger F, Drenkow J, Zaleski C, Jha S, et al. STAR: ultrafast universal RNA-seq aligner. Bioinformatics 2013;29:15–21. doi:10.1093/bioinformatics/bts635.
[35] Liao Y, Smyth GK, Shi W. featureCounts: an efficient general purpose program for

assigning sequence reads to genomic features. Bioinformatics 2014;30:923–30. doi:10.1093/bioinformatics/btt656.

[36] Robinson MD, McCarthy DJ, Smyth GK. edgeR: a Bioconductor package for differential expression analysis of digital gene expression data. Bioinformatics 2010;26:139–40. doi:10.1093/bioinformatics/btp616.

[37] Wang J, Shaner N, Mittal B, Zhou Q, Chen J, Sanger JM, et al. Dynamics of Z-band based proteins in developing skeletal muscle cells. Cell Motil Cytoskeleton 2005;61:34–48. doi:10.1002/cm.20063.

[38] Bollmann L, Koser DE, Shahapure R, Gautier HOB, Holzapfel GA, Scarcelli G, et al. Microglia mechanics: immune activation alters traction forces and durotaxis. Front Cell Neurosci 2015;9:363. doi:10.3389/fncel.2015.00363.

[39] Han SJ, Oak Y, Groisman A, Danuser G. Traction microscopy to identify force modulation in subresolution adhesions. Nat Methods 2015;12:653–6. doi:10.1038/nmeth.3430.

[40] Christ AF, Franze K, Gautier H, Moshayedi P, Fawcett J, Franklin RJM, et al. Mechanical difference between white and gray matter in the rat cerebellum measured by scanning force microscopy. J Biomech 2010;43:2986–92. doi:10.1016/j.jbiomech.2010.07.002.

[41] Avenarius MR, Krey JF, Dumont RA, Morgan CP, Benson CB, Vijayakumar S, et al. Heterodimeric capping protein is required for stereocilia length and width regulation. J Cell Biol 2017:jcb.201704171. doi:10.1083/jcb.201704171.

[42] Fu J, Wang Y-K, Yang MT, Desai RA, Yu X, Liu Z, et al. Mechanical regulation of cell function with geometrically modulated elastomeric substrates. Nat Methods 2010;7:733–6. doi:10.1038/nmeth.1487.

[43] Chang C-W, Kumar S. Differential Contributions of Nonmuscle Myosin II Isoforms and Functional Domains to Stress Fiber Mechanics. Sci Rep 2015;5:13736. doi:10.1038/srep13736.

[44] Murthy K, Wadsworth P. Myosin-II-Dependent Localization and Dynamics of F-Actin during Cytokinesis. Current Biology 2005;15:724–31. doi:10.1016/j.cub.2005.02.055.

[45] Dumbauld DW, Michael KE, Hanks SK, García AJ. Focal adhesion kinase-dependent regulation of adhesive forces involves vinculin recruitment to focal adhesions. Biol Cell 2010;102:203–13. doi:10.1042/BC20090104.

[46] Zhou DW, Lee TT, Weng S, Fu J, García AJ. Effects of substrate stiffness and actomyosin contractility on coupling between force transmission and vinculin-paxillin recruitment at single focal adhesions. Mol Biol Cell 2017;28:1901–11. doi:10.1091/mbc.E17-02-0116.

[47] Omachi T, Ichikawa T, Kimura Y, Ueda K, Kioka N. Vinculin association with actin cytoskeleton is necessary for stiffness-dependent regulation of vinculin behavior. PLoS ONE 2017;12:e0175324. doi:10.1371/journal.pone.0175324.

[48] Pasapera AM, Schneider IC, Rericha E, Schlaepfer DD, Waterman CM. Myosin II activity regulates vinculin recruitment to focal adhesions through FAK-mediated paxillin phosphorylation. J Cell Biol 2010;188:877–90. doi:10.1083/jcb.200906012.

[49] Shiu J-Y, Aires L, Lin Z, Vogel V. Nanopillar force measurements reveal actin-cap-mediated YAP mechanotransduction. Nat Cell Biol 2018. doi:10.1038/s41556-017-0030-y.

[50] Théry M, Racine V, Piel M, Pépin A, Dimitrov A, Chen Y, et al. Anisotropy of cell adhesive microenvironment governs cell internal organization and orientation of polarity. Proc Natl Acad Sci USa 2006;103:19771–6. doi:10.1073/pnas.0609267103.

[51] Schiller HB, Hermann M-R, Polleux J, Vignaud T, Zanivan S, Friedel CC, et al. β1-

and αv-class integrins cooperate to regulate myosin II during rigidity sensing of fibronectin-based microenvironments. Nat Cell Biol 2013;15:625–36. doi:10.1038/ncb2747.

[52] Aragona M, Panciera T, Manfrin A, Giulitti S, Michielin F, Elvassore N, et al. A mechanical checkpoint controls multicellular growth through YAP/TAZ regulation by actin-processing factors. Cell 2013;154:1047–59. doi:10.1016/j.cell.2013.07.042.

[53] Desai SS, Tung JC, Zhou VX, Grenert JP, Malato Y, Rezvani M, et al. Physiological ranges of matrix rigidity modulate primary mouse hepatocyte function in part through hepatocyte nuclear factor 4 alpha. Hepatology 2016;64:261–75. doi:10.1002/hep.28450.

[54] Moya IM, Halder G. The Hippo pathway in cellular reprogramming and regeneration of different organs. Curr Opin Cell Biol 2016;43:62–8. doi:10.1016/j.ceb.2016.08.004.

[55] Patel SH, Camargo FD, Yimlamai D. Hippo Signaling in the Liver Regulates Organ Size, Cell Fate, and Carcinogenesis. Gastroenterology 2017;152:533–45. doi:10.1053/j.gastro.2016.10.047.

[56] Yu F-X, Meng Z, Plouffe SW, Guan K-L. Hippo pathway regulation of gastrointestinal tissues. Annu Rev Physiol 2015;77:201–27. doi:10.1146/annurev-physiol-021014-071733.

[57] Lee J-H, Kim T-S, Yang T-H, Koo B-K, Oh S-P, Lee K-P, et al. A crucial role of WW45 in developing epithelial tissues in the mouse. Embo J 2008;27:1231–42. doi:10.1038/emboj.2008.63.

[58] Croci O, De Fazio S, Biagioni F, Donato E, Caganova M, Curti L, et al. Transcriptional integration of mitogenic and mechanical signals by Myc and YAP. Genes Dev 2017;31:2017–22. doi:10.1101/gad.301184.117.

[59] Zanconato F, Forcato M, Battilana G, Azzolin L, Quaranta E, Bodega B, et al. Genome-wide association between YAP/TAZ/TEAD and AP-1 at enhancers drives oncogenic growth. Nat Cell Biol 2015;17:1218–27. doi:10.1038/ncb3216.

[60] Jezowska B, Fernández BG, Amândio AR, Duarte P, Mendes C, Brás-Pereira C, et al. A dual function of Drosophila capping protein on DE-cadherin maintains epithelial integrity and prevents JNK-mediated apoptosis. Dev Biol 2011;360:143–59. doi:10.1016/j.ydbio.2011.09.016.

[61] Tarlow BD, Pelz C, Naugler WE, Wakefield L, Wilson EM, Finegold MJ, et al. Bipotential adult liver progenitors are derived from chronically injured mature hepatocytes. Cell Stem Cell 2014;15:605–18. doi:10.1016/j.stem.2014.09.008.

[62] Yanger K, Zong Y, Maggs LR, Shapira SN, Maddipati R, Aiello NM, et al. Robust cellular reprogramming occurs spontaneously during liver regeneration. Genes Dev 2013. doi:10.1101/gad.207803.112.

[63] Chen X, Calvisi DF. Hydrodynamic transfection for generation of novel mouse models for liver cancer research. The American Journal of Pathology 2014;184:912–23. doi:10.1016/j.ajpath.2013.12.002.

[64] Benhamouche S, Decaens T, Godard C, Chambrey R, Rickman DS, Moinard C, et al. Apc Tumor Suppressor Gene Is the “Zonation-Keeper” of Mouse Liver 2006;10:759–70. doi:10.1016/j.devcel.2006.03.015.

[65] Gougelet A, Torre C, Veber P, Sartor C, Bachelot L, Denechaud P-D, et al. T-cell factor 4 and β-catenin chromatin occupancies pattern zonal liver metabolism in mice. Hepatology 2014;59:2344–57. doi:10.1002/hep.26924.

[66] Gebhardt R, Matz-Soja M. Liver zonation: Novel aspects of its regulation and its impact on homeostasis. World J Gastroenterol 2014;20:8491–504. doi:10.3748/wjg.v20.i26.8491.

[67] Planas-Paz L, Orsini V, Boulter L, Calabrese D, Pikiolek M, Nigsch F, et al. The RSPO–LGR4/5–ZNRF3/RNF43 module controls liver zonation and size. Nat Cell Biol 2016;18:467–79. doi:10.1038/ncb3337.
[68] Gonzalez FJ, Kimura S. Understanding the role of xenobiotic-metabolism in chemical carcinogenesis using gene knockout mice. Mutat Res 2001;477:79–87.
[69] Lu L, Finegold MJ, Johnson RL. Hippo pathway coactivators Yap and Taz are required to coordinate mammalian liver regeneration. Exp Mol Med 2018;50:e423. doi:10.1038/emm.2017.205.
[70] Yi J, Lu L, Yanger K, Wang W, Hwa Sohn B, Stanger BZ, et al. LATS1 and LATS2 regulate mouse liver progenitor cell proliferation and maturation through antagonism of the coactivators YAP and TAZ. Hepatology 2016. doi:10.1002/hep.28768.
[71] Aylon Y, Gershoni A, Rotkopf R, Biton IE, Porat Z, Koh AP, et al. The LATS2 tumor suppressor inhibits SREBP and suppresses hepatic cholesterol accumulation. Genes Dev 2016. doi:10.1101/gad.274167.115.
[72] St John MA, Tao W, Fei X, Fukumoto R, Carcangiu ML, Brownstein DG, et al. Mice deficient of Lats1 develop soft-tissue sarcomas, ovarian tumours and pituitary dysfunction. Nature Genetics 1999;21:182–6. doi:10.1038/5965.
[73] Sorrentino G, Ruggeri N, Specchia V, Cordenonsi M, Mano M, Dupont S, et al. Metabolic control of YAP and TAZ by the mevalonate pathway. Nat Cell Biol 2014;16:357–66. doi:10.1038/ncb2936.
[74] Feng X, Degese MS, Iglesias-Bartolome R, Vaqué JP, Molinolo AA, Rodrigues M, et al. Hippo-independent activation of YAP by the GNAQ uveal melanoma oncogene through a trio-regulated rho GTPase signaling circuitry. Cancer Cell 2014;25:831–45. doi:10.1016/j.ccr.2014.04.016.
[75] Acton SE, Farrugia AJ, Astarita JL, Mourão-Sá D, Jenkins RP, Nye E, et al. Dendritic cells control fibroblastic reticular network tension and lymph node expansion. Nature 2014;514:498–502. doi:10.1038/nature13814.
[76] Haase K, Pelling AE. Investigating cell mechanics with atomic force microscopy. J R Soc Interface 2015;12:20140970. doi:10.1098/rsif.2014.0970.
[77] Meng Z, Qiu Y, Lin KC, Kumar A, Placone JK, Fang C, et al. RAP2 mediates mechanoresponses of the Hippo pathway. Nature 2018;560:655–60. doi:10.1038/s41586-018-0444-0.
[78] Elosegui-Artola A, Andreu I, Beedle AEM, Lezamiz A, Uroz M, Kosmalska AJ, et al. Force Triggers YAP Nuclear Entry by Regulating Transport across Nuclear Pores. Cell 2017;171:1397–1410.e14. doi:10.1016/j.cell.2017.10.008.
[79] Chang L, Azzolin L, Di Biagio D, Zanconato F, Battilana G, Lucon Xiccato R, et al. The SWI/SNF complex is a mechanoregulated inhibitor of YAP and TAZ. Nature 2018;563:265–9. doi:10.1038/s41586-018-0658-1.
[80] Fernández BG, Gaspar P, Brás-Pereira C, Jezowska B, Rebelo SR, Janody F. Actin-Capping Protein and the Hippo pathway regulate F-actin and tissue growth in Drosophila. Development 2011;138:2337–46. doi:10.1242/dev.063545.
[81] Sansores-Garcia L, Bossuyt W, Wada K-I, Yonemura S, Tao C, Sasaki H, et al. Modulating F-actin organization induces organ growth by affecting the Hippo pathway. Embo J 2011;30:2325–35. doi:10.1038/emboj.2011.157.
[82] Benham-Pyle BW, Pruitt BL, Nelson WJ. Mechanical strain induces E-cadherin-dependent Yap1 and -catenin activation to drive cell cycle entry. Science (New York, NY) 2015;348:1024–7. doi:10.1126/science.aaa4559.
[83] Moroishi T, Hayashi T, Pan W-W, Fujita Y, Holt MV, Qin J, et al. The Hippo Pathway Kinases LATS1/2 Suppress Cancer Immunity. Cell 2016;167:1525–1539.e17. doi:10.1016/j.cell.2016.11.005.

FIGURE LEGENDS

Figure 1. The F-actin capping protein *Capzb* regulates cellular forces *in vitro*

(A) Representative pictures of control (*WT*) and *CAPZ KO* mouse adult fibroblasts (MAFs) plated for 24 hours on microprinted fibronectin-coated islands of the indicated adhesive area and stained for YAP/TAZ and EdU incorporation. Quantification of nuclear YAP/TAZ on the right. n=2 (>100 cells per condition in total). Scale bar = 10µm.

(B) Quantification of proliferation in MAFs plated as in A, as assayed by EdU incorporation. n=2 (>100 cells per condition in total).

(C) Representative high-magnification immunofluorescent stainings for F-actin bundles (Phalloidin) in the cytoplasm of *WT* and *Capzb*-null MAFs. n=3 with consistent results. Scale bar = 3µm.

(D) and (E) FRAP (fluorescence recovery after photobleaching) analysis of *WT* and *Capzb*-null MAFs transfected with GFP-Actin (D) or mCherry-Vinculin (E), indicated as mean and s.e.m. **Inset**: half-time (t1/2) and 95% Confidence Interval of Actin recovery calculated by fitting the data to a monoexponential function. See Supplementary Figure 1E-F for representative images. n=2 (D: >25 cells per condition in total; E: >40 cells per condition in total). Scale bar = 1.5µm.

(F) and (G) Quantification of the number (F) and size (G) of focal adhesions by TIRF (total internal reflection fluorescence) of MAFs transfected with mCherry-Vinculin. See Supplementary Figure 1G for representative images. n=2 (16 cells per condition).

(H) Average F-actin (Phalloidin) and Vinculin immunofluorescence stainings in *WT* and *Capzb*-null MAFs plated on cross-bow fibronectin-coated micropatterns. Immunofluorescence of multiple individual cells on ECM micropatterns were stacked (n=25 per condition); the resulting image shows the average pixel intensity as a multicolor look-up table. Scale bar = 5µm.

(I) Traction force analysis of *WT* and *Capzb*-null MAFs plated on stiff (G'=10kPa) fibronectin-coated polyacrylamide hydrogels. n=2 (50 cells per condition). **Left**: representative force maps with cell and nucleus contour overlaid. Local force is indicated by a multicolor look-up table. **Right**: box plot (median, quartiles and extremes). n=3 (50 cells per condition).

(J) Representative immunofluorescent stainings for pMLC and F-actin bundles (Phalloidin) in *WT* and *Capzb*-null MAFs plated on soft (G'=1kPa) hydrogels. **On the right**: quantification of cells displaying pMLC staining. n=3 (80 cells per condition). Scale bar = 3µm.

(K). Traction force analysis of *WT* and *Capzb*-null fibroblasts plated on soft (G'=1kPa) hydrogels. Box plot (median, quartiles and extremes). n=3 (50 cells per condition).

Unless otherwise indicated, graphs are average and single points with unpaired two-tailed Student's t-test. Immunostainings were repeated in independent experiments, and a representative result is shown.

Figure 2. *Capzb* restricts YAP activity, prevents liver overgrowth and maintains adult hepatocyte quiescence

(A) Immunostaining for endogenous CAPZB in liver sections from control (*WT*) and *CAPZ LKO* mice. Asterisks indicate non-hepatocyte cells that remain positive for CAPZB. Occasional patches of non-recombined cells (*WT*, white dotted line) surrounded by the *Capzb*-null tissue (positive for β-galactosidase) serve as internal control. Scale bar =20µm.

(B) Expression of established YAP/TAZ target genes, as measured by RNA sequencing of whole livers from control and *CAPZ LKO* mice . Average expression levels in control (*WT*) mice was arbitrarily set equal to 1, and all other data are relative to this. n=4 for each genotype.

(C) Similarity matrix between *Capzb* liver knockouts, *Hippo* liver knockouts (Mst1/2 a[78] b[28], Sav1/WW45[78], Lats1/2[26]), *Yap* liver transgenics (Tg a[60] b[18] c[20]), and an unrelated liver knockout (outlier[79]). Coefficients were calculated for the indicated pairwise comparisons based on genes significantly overexpressed (fold>1.5; $P \leq 0.05$).

(D) Left: representative Immunostaining for YAP in liver sections from control (*WT*) or *CAPZ LKO* mice. DAPI serves as nuclear counterstain. Scale bar = 10µm. **Right**: quantification of hepatocytes displaying nuclear YAP. n=3 for each genotype.

(E) Low magnification YAP immunofluorescence in a liver section from a *CAPZ LKO* mouse with occasional non-recombined hepatocytes (*WT*). n=3 mice were consistent. Scale bar = 20µm.

(F) Representative pictures of control (*WT*) and *CAPZ LKO* livers upon dissection. On the right: quantification of body/liver weight ratio (see also Supplementary Table 1). n=9 for each genotype.

(G) and (H) Representative stainings for EdU (G, n=3 for each genotype) and phospho-Histone3 (H, n=2 for each genotype) and their quantifications. Scale bars = 10µm.

(I) Expression of proliferation marker genes as measured by RNA sequencing of whole livers from control and *CAPZ LKO* mice. Average expression levels in control (*WT*) mice was arbitrarily set equal to 1, and all other data are relative to this. n=4 for each genotype.

Graphs are average and single points (mice) with unpaired two-tailed Student's t-test with Welch's correction. Immunostainings were repeated in independent sections of independent mice (see methods), and a representative result is shown.

Figure 3. *Capzb* is required to maintain hepatocyte cell differentiation

(A) Representative hematoxylin and eosin (H&E, left) and immunostainings for the atypical ductal cell markers CK19 and A6 (center and right) in control (*WT*) and *CAPZ LKO* liver sections. Quantification of the CK19-positive area in sections containing the portal area. n=3 per genotype. Scale bar = 100µm.

(B) Expression of liver progenitor/cholangiocyte markers as measured by RNA sequencing of whole livers from control and *CAPZ LKO* mice . Average expression levels in control (*WT*) mice was arbitrarily set equal to 1, and all other data are relative to this. n=4 for each genotype.

(C) Appearance of cells double-positive for differentiated hepatocyte (HNF4α) and atypical ductal cell (CK19) markers in *CAPZ LKO* livers. Scale bar = 5µm. Quantification in sections of the portal area. n=3 for each genotype. ** $P<0.01$.

(D) Expression of Notch pathway and Notch target genes as measured by RNA sequencing of whole livers from control and *CAPZ LKO* mice . Average expression levels in control (*WT*) mice was arbitrarily set equal to 1, and all other data are relative to this. n=4 for each genotype.

(E) Representative immunostainings for HES1 in control (*WT*) and *CAPZ LKO* liver sections. HES1 is restricted to bile duct cells (asterisks) in *WT* mice. Co-localization with HNF4α (arrowheads) was only observed in *CAPZ LKO* mice. Scale bar = 15µm.

(F) Double immunofluorescence for CK19 and β-galactosidase (used as hepatocyte lineage tracer) in *CAPZ LKO* livers (*whole liver KO*). Quantification in sections not containing the portal area. Scale bar = 30µm.

(G) Double immunofluorescence for CK19 and β-galactosidase (used as hepatocyte lineage tracer) in *Capzb-fl/fl; ROSA26-LSL-lacZ* mice with live HTV injection of Cre transposon plasmid, inducing recombination in single hepatocytes. Scale bar = 15µm.

Graphs are average and single points (mice) with unpaired two-tailed Student's t-test with Welch's correction. Immunostainings were repeated in independent sections of independent mice (see methods), and a representative result is shown.

Figure 4. *Capzb* controls hepatocyte zonation and liver metabolism

(A) Expression of pericentral hepatocyte marker genes as measured by RNA sequencing of whole livers from control and *CAPZ LKO* mice . Average expression levels in control (*WT*) mice was arbitrarily set equal to 1, and all other data are relative to this. n=4 for each genotype.

(B) and (C) Immunofluorescence for the pericentral hepatocyte markers GS (glutamine synthase - B) and CYP8B1 (C) on liver sections from control (*WT*) and *CAPZ LKO* mice, in the region of the central vein. Scale bar = 80µm (B), 120µm (C).

(D) Analysis of cell death by TUNEL staining of pericentral liver sections (left: representative stainings; right: quantification) in control (*WT*) and *CAPZ LKO* mice 24 hours after injection with a toxic dose of acetaminophen (APAP). n=2 mice for each genotype. Scale bar = 80µm

(E) Serum alanine aminotransferase (ALT) levels was measured from sera of mice 8 hours after APAP injection, as in (D) n=2 mice for each genotype.

(F) Expression of gluconeogenesis enzymes as measured by RNA sequencing of whole livers from control and *CAPZ LKO* mice . Average expression levels in control (*WT*) mice was arbitrarily set equal to 1, and all other data are relative to this. n=4 for each genotype.

(G) Glucose tolerance test after intraperitoneal injection in control (*WT*) and *CAPZ LKO* mice. Statistical significance was calculated on the area under the curve (AUC) values.

Average and s.e.m. n≥4 mice for each genotype.

Graphs are average and single points (mice) or s.e.m. with unpaired two-tailed Student’s t-test with Welch’s correction. Immunostainings were repeated in independent sections of independent mice (see methods), and a representative result is shown.

Figure 5. *Capzb* regulates liver homeostasis through *YAP1* and in parallel to Hippo

(A) Liver/body weight ratio of the indicated *CAPZ LKO*, *CAPZ+YAP LKO* (n>6 for each genotype) and *YAP LKO* mice (n=3).

(B) EdU incorporation in the indicated mice. n=3 for each genotype.

(C) and (D) Representative immunofluorescence for the atypical ductal cell marker CK19 (C) and for the pericentral marker GS (D) on liver sections from the indicated mice. n=3 mice were consistent for each staining. Scale bar = 100µm (C), 80µm (D).

(E) Glucose tolerance test upon intraperitoneal injection as measured by glucose area under the curve (AUC) in mice of the indicated genotypes. *WT* are control mice.

(F) Quantification of EdU incorporation in control livers (*Capzbfl/fl; ROSA26-LSL-lacZ* mice injected with GFP transposon), in livers with single-cell inactivation of *Capzb* (*CAPZ CRE*: *Capzbfl/fl; ROSA26-LSL-lacZ* mice injected with CRE transposon), with single-cell inactivation of *Lats1/2* (*Lats1/2 CAS9*: *Capzbfl/fl; ROSA26-LSL-lacZ* mice injected with RFP-Lats1/2-gRNA and CAS9-expressing transposon), or their combination. Hepatocytes were transduced by hydrodynamic tail vein injection. n=3 for each genotype. See Supplementary Fig. 3E for representative stainings.

(G) Quantification of EdU incorporation in control and *CAPZ LKO* livers injected with GFP or with TAZ-4SA transposons. Hepatocytes were transduced by hydrodynamic tail vein injection. n=2 for each genotype. See Supplementary Fig. 3F for representative stainings.

Graphs are average and single points (mice) with unpaired two-tailed Student's t-test with Welch's correction. Immunostainings were repeated in independent sections of independent mice (see methods), and a representative result is shown.

Figure 6. *Capzb* regulates liver homeostasis and YAP by modulating hepatocyte contractility

(A) Representative immunofluorescence stainings for phosphorylated myosin-light-chain (pMLC), F-actin (Phalloidin) and β-galactosidase (recombined cells) in a *CAPZ LKO* liver section. *WT* indicates non recombined hepatocytes. n=3 mice were consistent. Scale bar = 20µm.

(B) Atomic force microscopy (AFM) analyses were performed on control (*WT*) and *CAPZ LKO* livers. **Left**: Representative AFM maps, with squares corresponding to single adjacent measurements. **Right:** Box plot (median, quartiles and extremes). n>4 maps from 2 mice of each genotype.

(C) Expression of hepatocyte mechano-responsive genes as measured by RNA sequencing of whole livers from control and *CAPZ LKO* mice. Average expression levels in control (*WT*) mice was arbitrarily set equal to 1, and all other data are relative to this. n=4 for each genotype.

(D) Representative immunofluorescence stainings for phosphorylated myosin-light-chain (pMLC) on liver sections of mice of the indicated genotypes treated without or with the Fasudil ROCK-inhibitor (ROCKi). n=3 mice were consistent. Scale bar = 80µm.

(E) Expression of YAP target genes as measured by qPCR of whole livers from control (*WT*) and *CAPZ LKO* mice without or with Fasudil (ROCKi). Gene levels relative to *GAPDH*. Average expression levels in control mice was arbitrarily set equal to 1, and all other data are relative to this. n=4 for *CAPZ LKO* +/- ROCKi.

(F) and (G) Quantification of EdU incorporation (F) and CK19-positive atypical ductal cells (G) in livers from control (*WT*) and *CAPZ LKO* mice treated without or with Fasudil (ROCKi). n=4 for *CAPZ LKO* +/- ROCKi.

Graphs are average and single points (mice) with unpaired two-tailed Student's t-test with Welch's correction. Immunostainings were repeated in independent sections of independent mice (see methods), and a representative result is shown.

JHEPAT-D-18-01600

Highlights

- Absence of CAPZ leads to increased cell contractility and tissue stiffness

- Loss of CAPZ leads to liver overgrowth, hepatocyte reprogramming and metabolic defects
- These phenotypes are due to YAP hyperactivation, and occur in parallel to LATS1/2
- ROCK inhibition rescues the effects of CAPZ inactivation
- Loss of CAPZ unveils the relevance of mechanical signals for tissue homeostasis

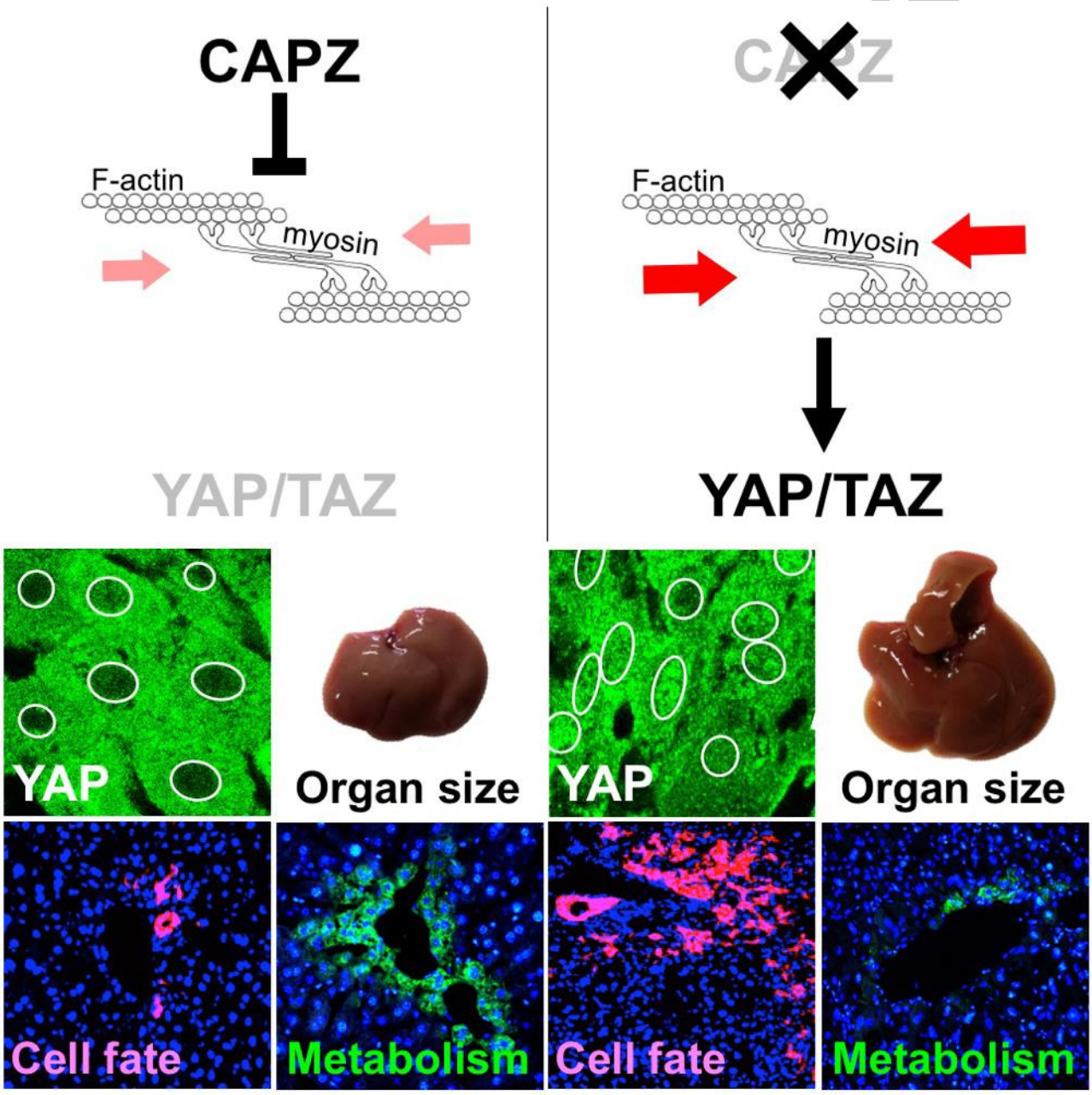

Pocaterra - Figure 1

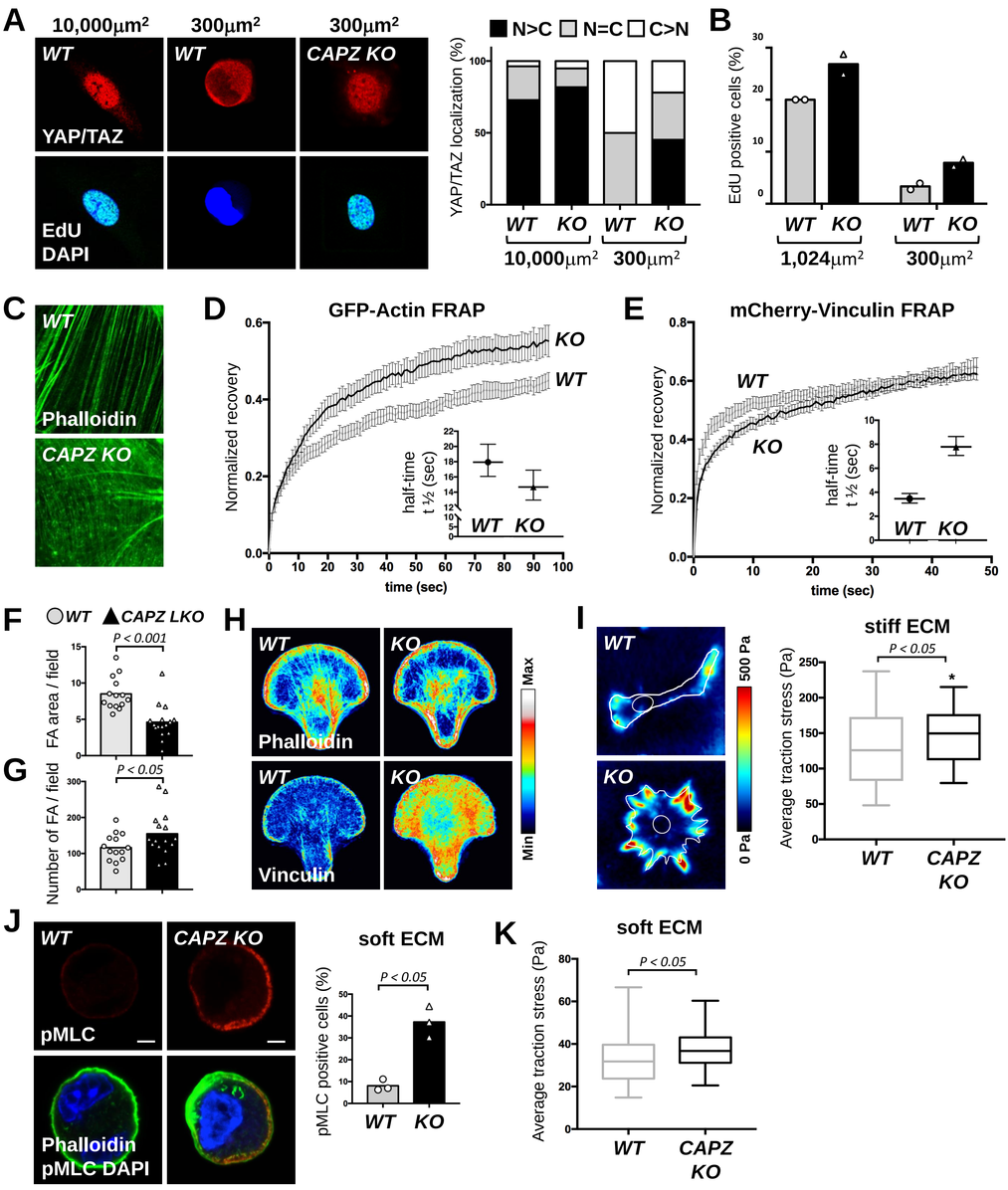

Figure 2

Pocaterra - Figure 2

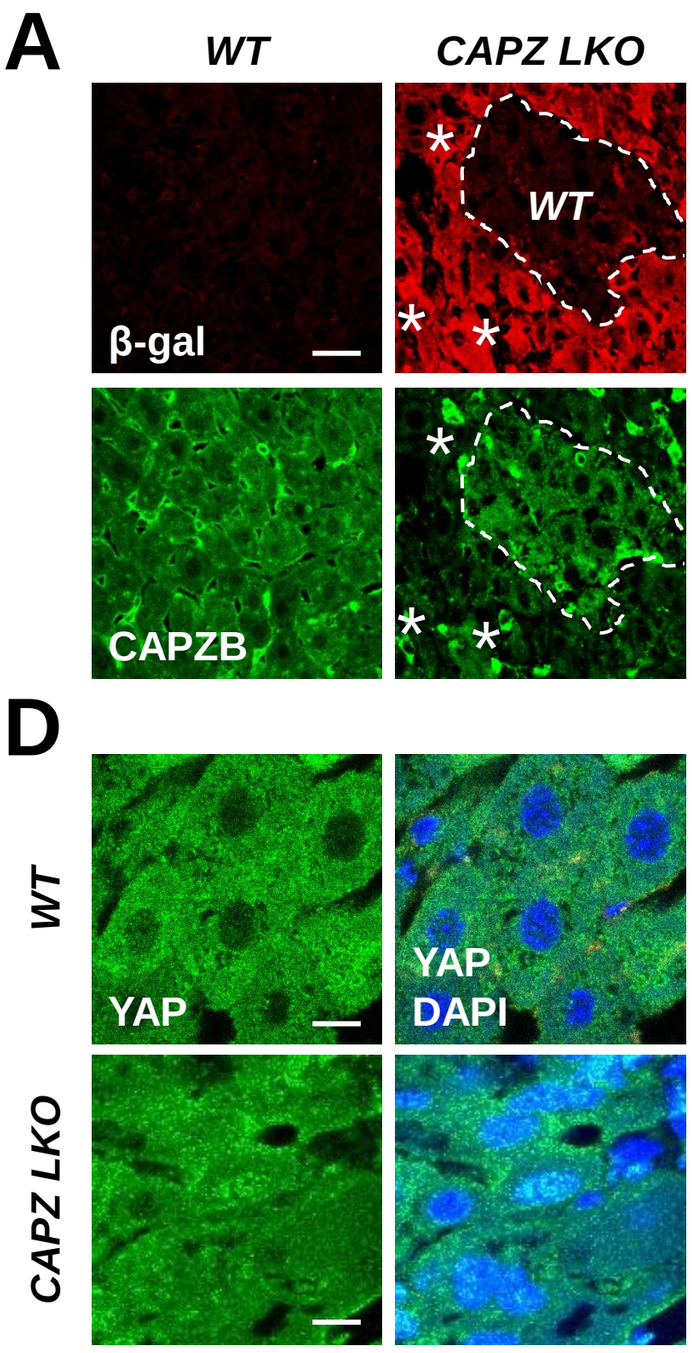

Figure 3

Pocaterra - Figure 3

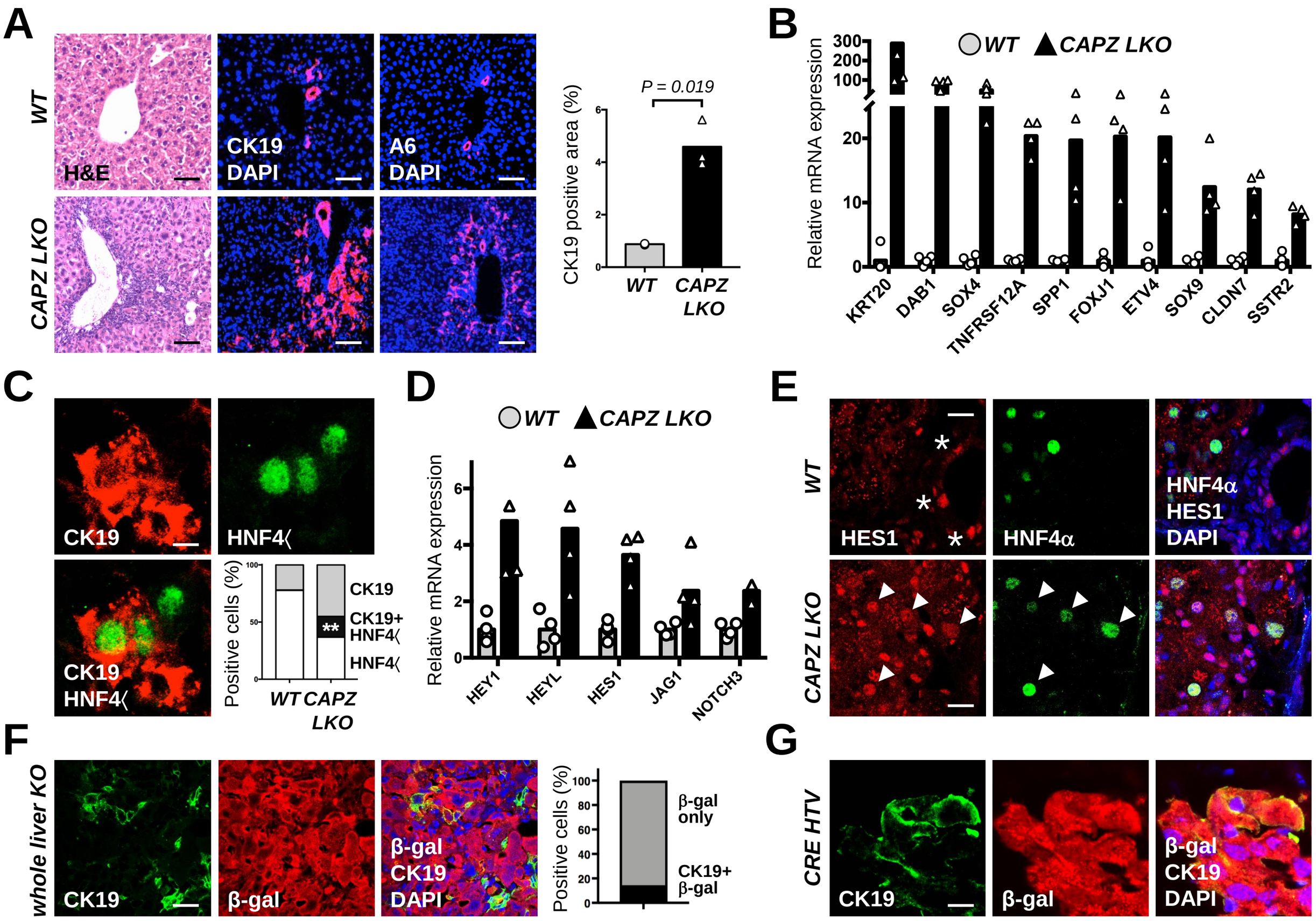

Figure 4

Pocaterra - Figure 4

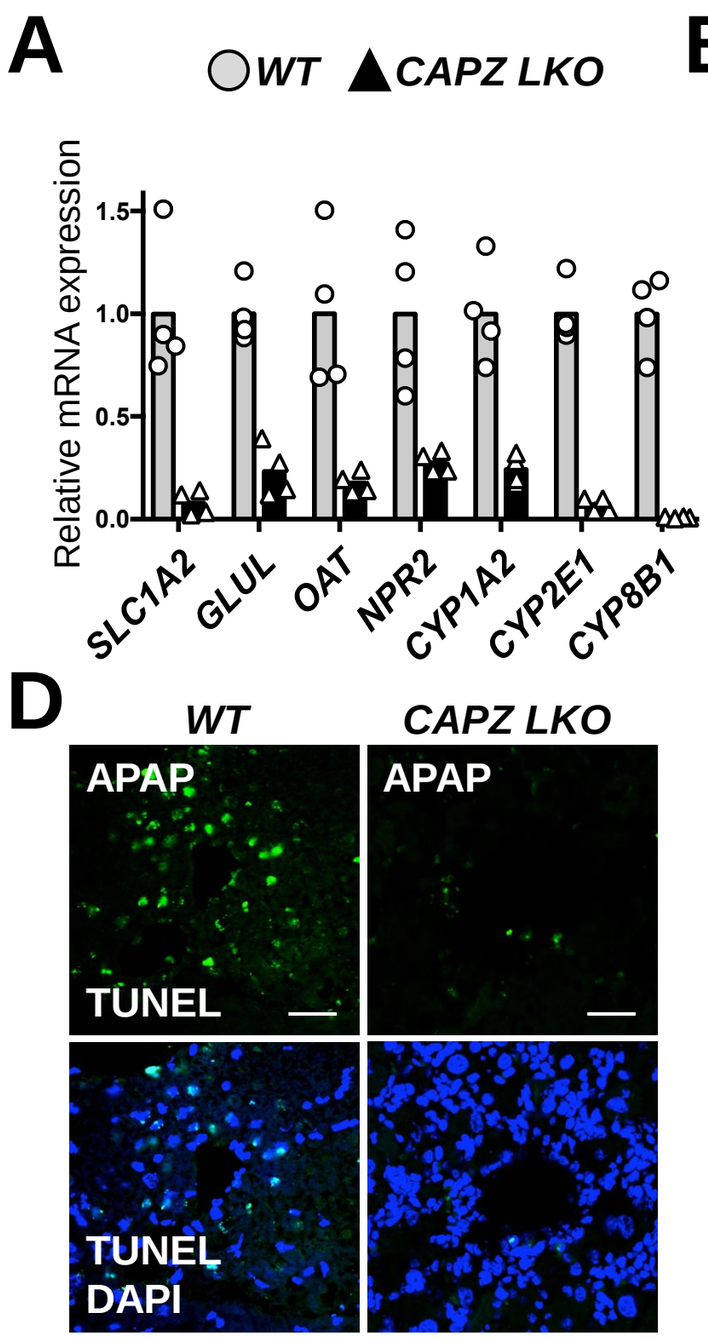

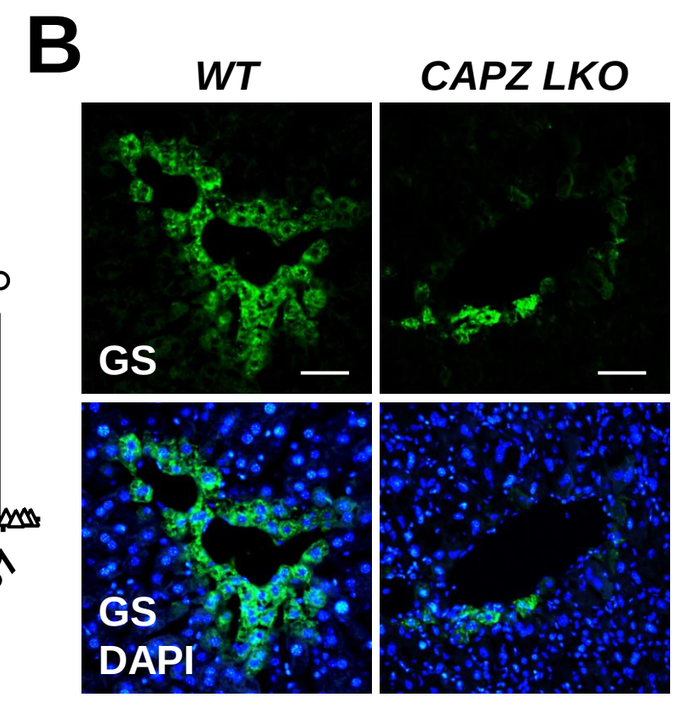

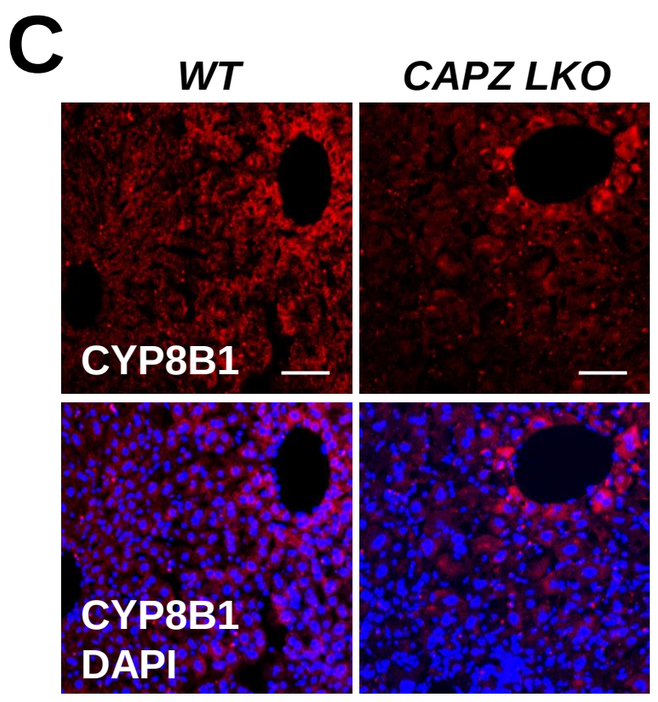

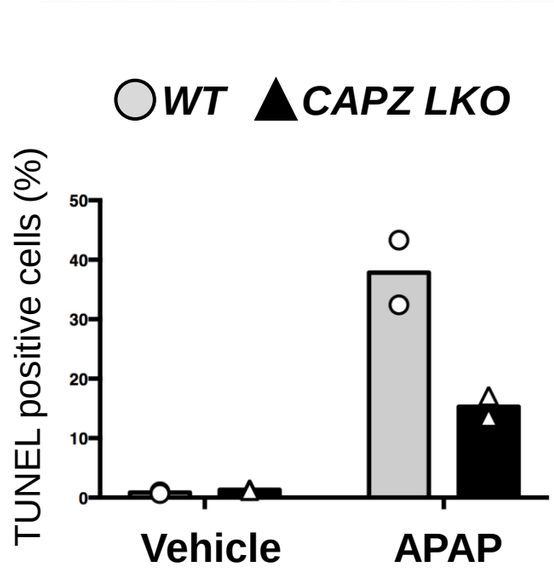

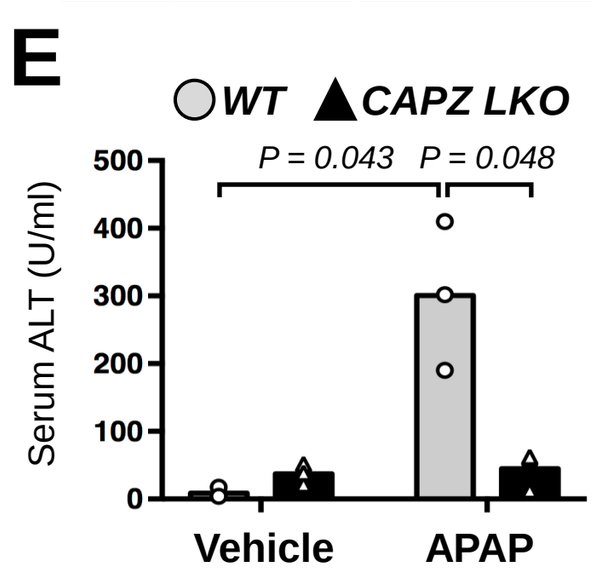

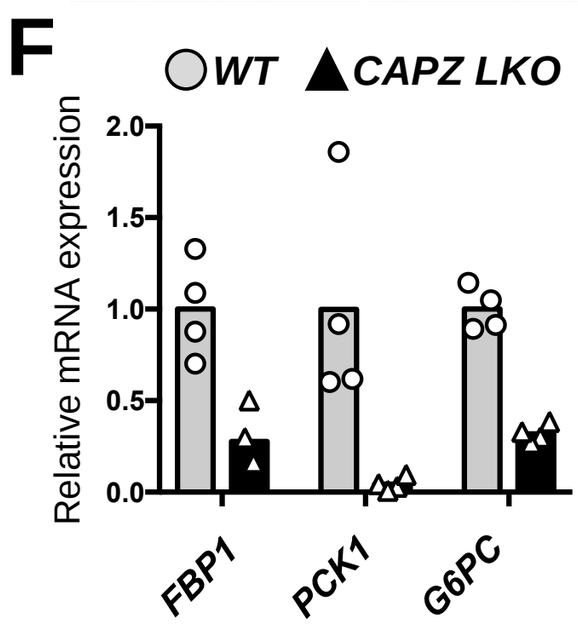

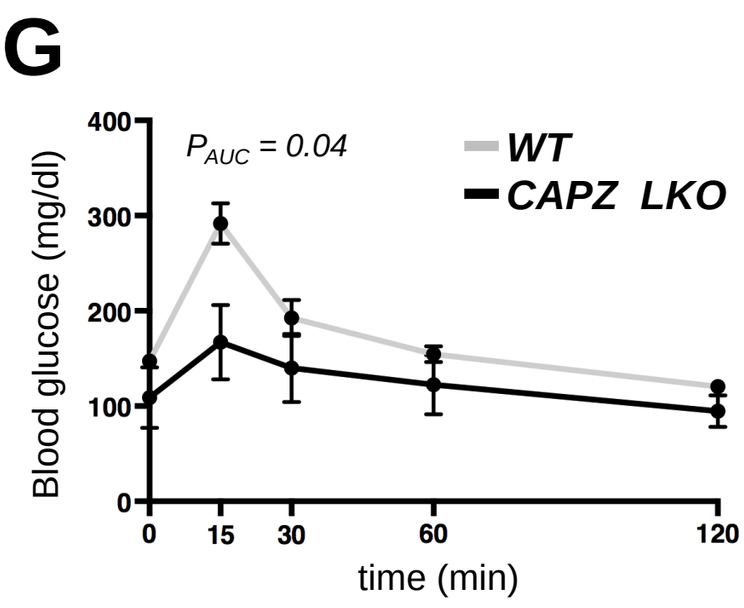

Figure 5

Pocaterra - Figure 5

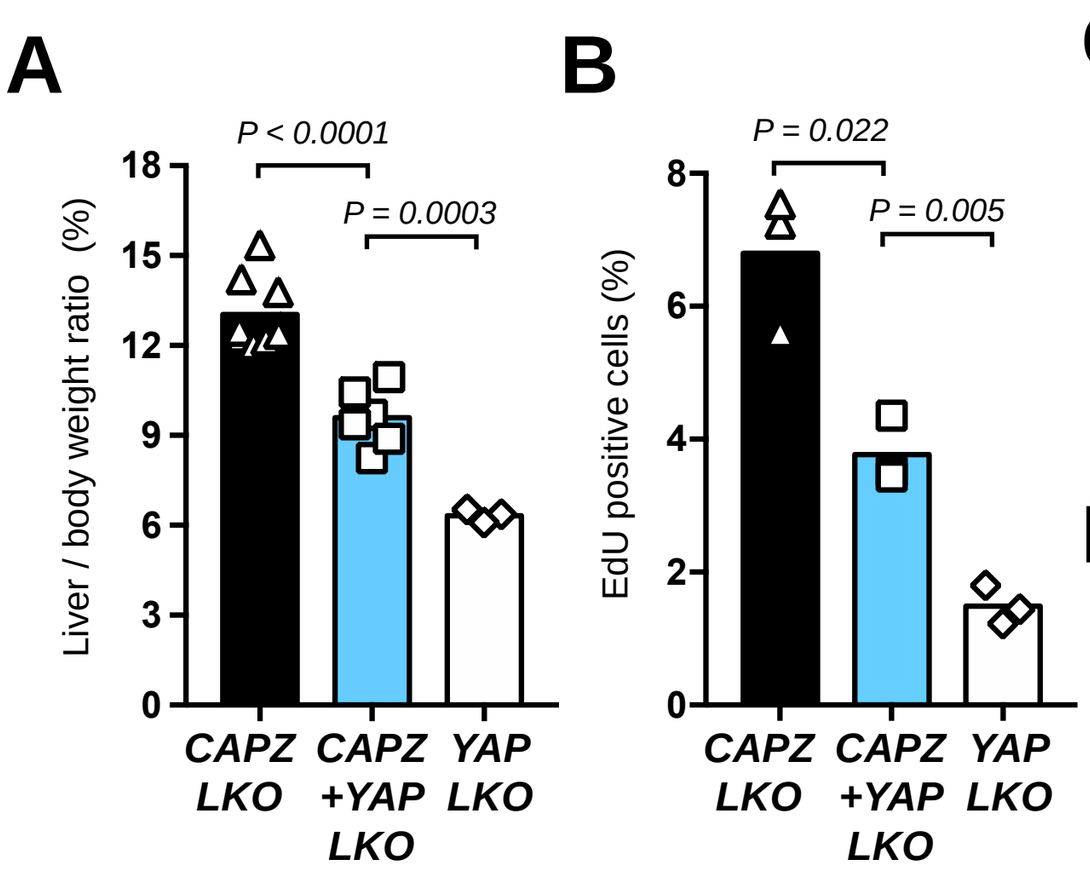

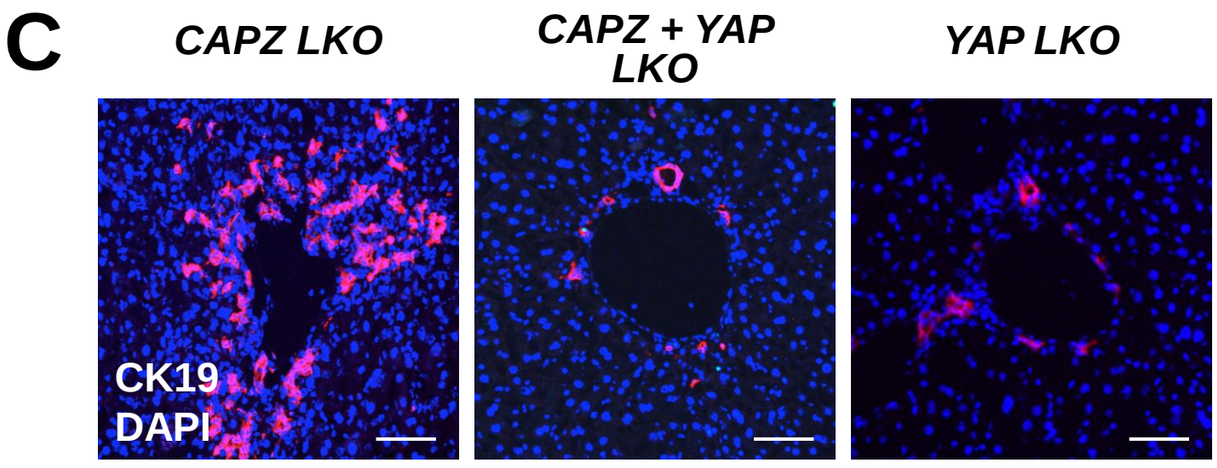

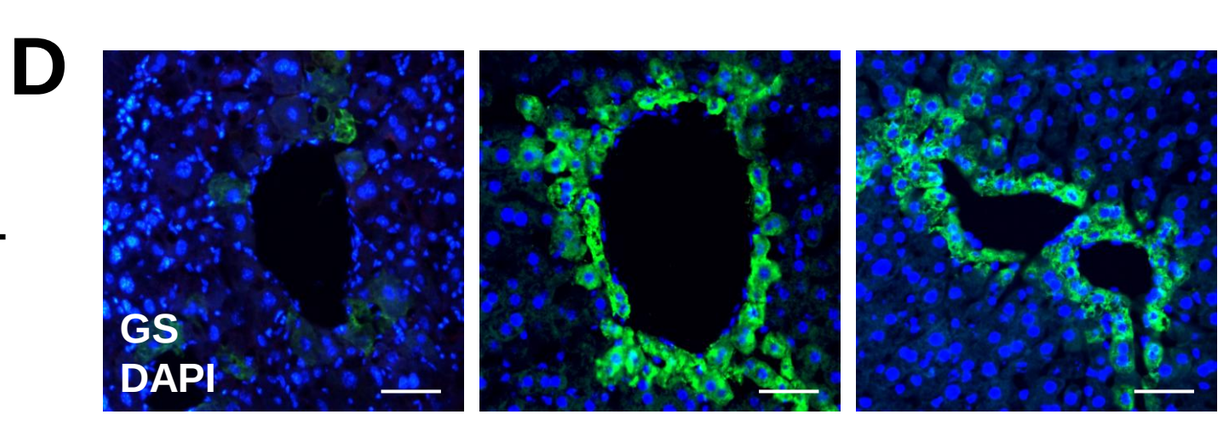

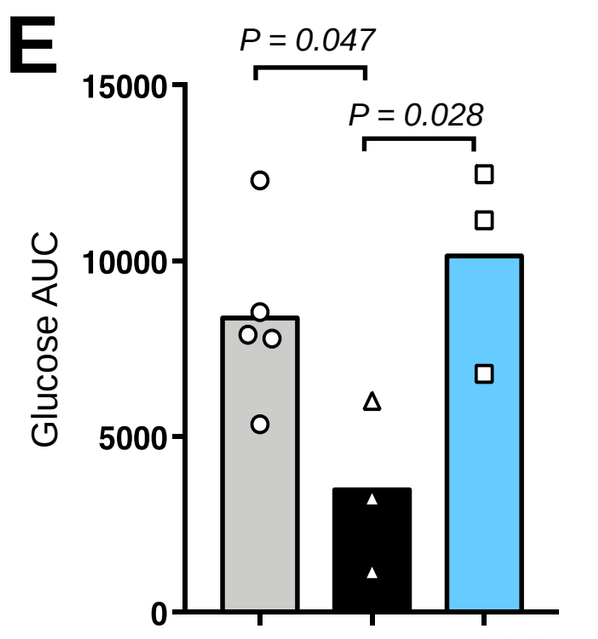

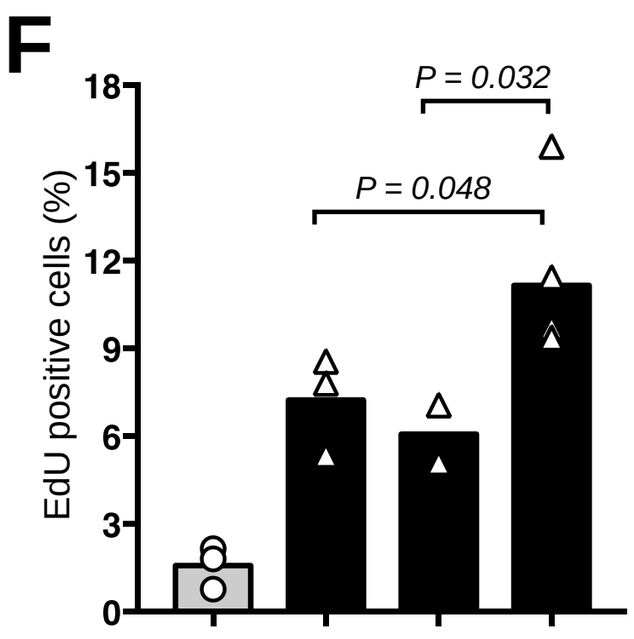

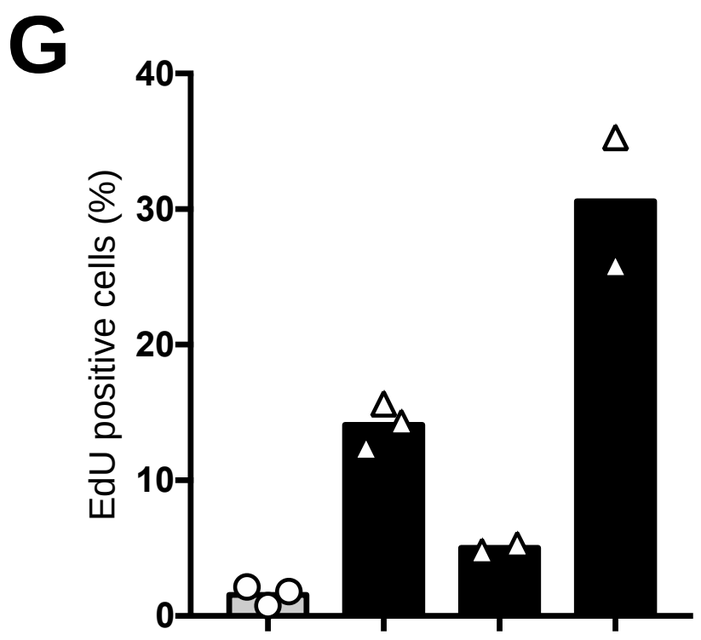

WT	CAPZ LKO	CAPZ +YAP LKO	CAPZ CRE Lats1/2 CAS9	+		+	CAPZ LKO	+		+
					+	+			+	+
							TAZ 4SA			

Figure 6

Pocaterra - Figure 6